Fall 1-31-1997

Experimental investigation of collisional properties of spheres

Laurent Labous
New Jersey Institute of Technology

ABSTRACT

EXPERIMENTAL INVESTIGATION
OF COLLISIONAL PROPERTIES
OF SPHERES

by
Laurent Labous

We present experimental results on the collisional properties of spheres obtained through high-speed video analysis. An apparatus is built that produces collisions of spheres of various sizes with a wide range of impact velocities and incidence angles.

Edge detection techniques are implemented to track the position of the spheres from frame to frame whereby the translational velocities may be computed. In order to determine the rotational velocities, small markers are imprinted on the surfaces of the spheres and also tracked and matched from one frame to the next. From the pre and post collision kinematic data, three collisional properties are directly extracted: the coefficient of restitution in the normal direction of impact, the coefficient of friction and the coefficient of restitution of the relative tangential velocity. These measurements substantiate an existing impact model predicting exclusively *rolling* and *sliding* collisions.

Finally the dependence of the coefficient of restitution on the magnitude of the normal impact velocity is studied for two different materials which both exhibit different behaviors from what available theoretical results predict. We could not observe any size dependence of the coefficient of restitution. This is due to the limited accuracy of our measurements but also to the possible sensitivity of the coefficient of restitution to the angle of incidence. However softer materials should provide more conclusive results.

EXPERIMENTAL INVESTIGATION OF
COLLISIONAL PROPERTIES OF SPHERES

by
Laurent Labous

A Thesis
Submitted to the Faculty of
New Jersey Institute of Technology
in Partial Fulfillment of the Requirements for the Degree of
Master of Science in Mechanical Engineering

Department of Mechanical Engineering

January 1997

Blank Page

APPROVAL PAGE

EXPERIMENTAL INVESTIGATION
OF COLLISIONAL PROPERTIES
OF SPHERES

Laurent Labous

Dr. Anthony D. Rosato, Thesis Advisor   Date
Associate Professor of Mechanical Engineering, NJIT

Dr. Rajesh N. Dave, Committee Member   Date
Associate Professor of Mechanical Engineering, NJIT

Dr. Denis Blackmore, Committee Member   Date
Professor of Mathematics, NJIT

BIOGRAPHICAL SKETCH

Author: Laurent Labous

Degree: Master of Science

Date: October 1996

Undergraduate and Graduate Education:

- Master of Science in Mechanical Engineering,
  New Jersey Institute of Technology,
  Newark, New Jersey, 1996

- Master of Science in Mechanics,
  Université Pierre et Marie Curie,
  Paris, France, 1992

- Bachelor of Science in Physics,
  E.N.S.,
  Paris, France, 1990

Major: Physics

ACKNOWLEDGMENT

TABLE OF CONTENTS

TABLE OF CONTENTS
(Continued)

LIST OF FIGURES

LIST OF FIGURES
(Continued)

CHAPTER 1

INTRODUCTION

1.1   Introduction

Bulk solids or granular materials consist of a collection of solid components of macro-
scopic sizes immersed in a fluid. These materials are present in nature in a variety
of common forms like sand or pebbles on a beach, cereal seeds in a hopper, coal
and slurries. They also appear in geophysical phenomena like dunes, avalanches
or landslides, mudflows, pack ice flows etc. These flows can develop a tremendous
amount of energy and cause catastrophic damage. Huge quantities of grains or
powder have sometimes to be handled in industrial processes where efficient mixing,
conveying or storage techniques have to be used that are still under development.
Although they appear in nature in simple forms they do exhibit very complex and
diverse static or dynamic behaviors. The first scientific investigations on granular
matter were carried out in the 19th century. The pionneering work of Reynolds [1]
evidenced the tendency of a compact assembly of grains under shearing to dilate. In
recent years granular materials have motivated significant research efforts: because
bulk solids occupy such a preponderant place in human activities and environment,
and have so many economical consequences, engineering design solutions cannot
afford to rely on error and trial development methods. In the past 15 years attention
has been focused on microstructural level studies that in turn allow for quantitative
predictions of large scale flows. Hence, more fascinating phenomena have been inten-
sively studied. Typical examples [2] are size-segregation [3, 4, 5, 6, 7] , convection
[8], surface waves [9, 10] and heap formation [11, 12]. However, both the physics
and mechanics of bulk materials are nowadays still not well understood: their study
requires the use of concepts pertaining to general physics , condensed matter physics
as well as fluid and solid mechanics , soil mechanics and rheology.

1

Granular flows are characterized by their highly nonlinear nature and often comprise fluid-like and solid-like behavior, therefore making the development of constitutive equations describing their behavior over a wide range of conditions a challenging goal. Consequently, the need for a classification of granular flows has grown. Bagnold [13] proposed a quantitative one, based on his experimental observations of an assembly of monodisperse, neutrally buoyant wax spheres bathed in a Newtonian fluid and sheared in a coaxial cylindrical cell. He distinguished three different regimes according to the relative importance of momentum fluxes arising in the fluid phase and those due to the collisional interactions between grains. He termed as *macro-viscous* the regime where viscosity was dominant and the stress proportional to the shear rate as for a Newtonian fluid. At the other extreme of his scale, where the role played by the interstitial fluid was negligible, he found a *grain-inertia* regime: in this case stress is created, according to Bagnold, as a result of a succession of glancing collisions due to the difference in transport velocities of two adjacent sheared layers. Here the shear stress should be proportional to the square of the shear rate since both the collision frequency and the momentum exchange during one single collision are proportional to the relative velocity of the two layers. In the case of a dry cohesionless granular material the situation is a little different because other mechanisms for stress generation can appear. (For a review see for example [14]). At high shear rate a *grain-inertia* regime is expected and the solids fraction may be high enough so that the same mechanisms of stress generation occurs. This is similar to the "hard-sphere" kinetic theory models of dense fluids. However, if the solids fraction is low enough, momentum may also be transported by particles moving due to their fluctuation velocity around the mean flow, from one layer to the next because there is enough void volume to do so. This is the situation encountered in kinetic theory of very dilute gases. For low shear rates and high solids concentrations, particles will experience enduring frictional contacts: this is a quasi-static regime

with Coulomb-type, rate-independent stresses. For low concentrations, particles will be able to travel freely on an average distance much larger than their typical diameter and stress will be generated by the interchanges of particles between different layers having different transport velocities. For engineering applications, but also natural flows, it is likely that both instantaneous collisions and enduring contacts will be encountered within the same flow. Understanding of the collision process between two granules therefore plays a crucial role in the knowledge of the stress tensor and tranport coefficients in rapid granular flows.

Owing to the complex nature of any granular flow, advances in computers has made simulations to study flows feasible. Numerical simulations of bulk solids have been turned into a very powerful widely used tool [15], trying to make up for the difficulty to make any direct, noninvasive physical measurements in real experiments, to complement existing experimental results and test theoretical ones [16, 17, 18, 19, 20, 21]. They provide a means whereby the sensitivity of theoretical models may be tested and validated in the absence of experimental data. Among other computational techniques molecular dynamics [22] and event-driven algorithms [23, 24, 25, 26] have been used extensively during the past 25 years. Granular flows are also studied on the basis of fluid mechanics [27], or, due to their similarity with gases in the *grain-inertia* regime, kinetic theory models of dilute and dense gases. [28, 29] However a distinctive property of grains is that their collisions are inherently inelastic. Mechanisms generating energy losses and/or transfers during collisions are extremely complicated but have to be somehow included in a proper approximation of collisions because they constitute a major factor in the complexity of granular flows. For simplicity, grains are usually idealized as disks or spheres sometimes with different shapes such as ellipses. But even the basic problem of the impact of two identical frictional spheres is not completely solved. Binary collisions are modeled either by some force scheme acting during collision only or by some

collision operator where the contact time is implicitly assumed to be zero. In both cases, the corresponding output is sometimes highly dependent on the collision model used [18, 30, 31, 32], so it has to be used with much care and must be ultimately validated through experiment.

The work which will be presented here will precisely focus on the problem of providing experimental validation.

1.2 Outline of the Remaining Chapters

In Chapter 2, we will go through a literature review in the fields of contact and collision mechanics related to our own work (i.e. the impact of spheres). This will provide some insight on the complexity of the mechanisms involved in a collision between elastic frictional spheres and how they may be modeled. Available theoretical and experimental results as well as different experimental approaches which have been used to investigate collision properties of spheres will also be presented. A brief review of the recent use of image analysis as a non-invasive technique in the study of physics of granular materials will be done. The theoretical foundation of our work will be laid in Chapter 3. Chapter 4 describes our experimental apparatus and method. Finally experimental results are presented and discussed in Chapter 5.

CHAPTER 2

LITERATURE REVIEW

2.1 Introduction

As it was suggested in the previous Chapter, the peculiarity of granular flows stems from the way particulates act on each other when they come into contact. Both numerical simulations and theories rely on the specification of interactions laws. For *Molecular Dynamics* kind of simulations some force scheme will be prescribed acting during the time two particulates are in contact, whereas for *Event-Driven* simulations or kinetic theories the pre- and post-collision kinematics of the grains are related by an instantaneous operator. Each of these techniques involves parameters that have to be linked to mechanical properties of real materials for the forthcoming results to be validated and compared with others. For pratical purposes, particulates are often idealized as homogeneous and isotropic spheres. Throughout this thesis we will focus on this particular case. However, even though the problem of the impact of two elastic spheres has not been completely solved, the advances that have been made since the early work of Hertz have brought much insight in the processes involved so they can now be modeled reasonably well. Yet, any model requires experimental validation to insure that realistic values of material properties are used. This data is still scarce although some efforts have been made using video analysis techniques to track the motion of colliding/flowing spheres.

2.2 The Mechanics of Elastic Spheres in Contact

Hertz [33] first considered the case of two elastic isotropic spheres pressed together by a force parallel to the line joining their centers. By solving the relevant elasticity equations, he obtained the relative approach of the two bodies and the pressure distribution across the surface during the contact as well as the duration of the contact. His analysis is quasi-static in the sense that the region where the elastic deformation

occurs is constantly in thermodynamic equilibrium and does not loose energy through elastic vibration. Some of these predictions were verified experimentally [34, 35] and the quasi-static assumption has been checked theoretically [36].

Based on Hertz's theory, and assuming the same normal stress distribution in the contact surface, Mindlin tackled the case of oblique contact between elastic frictional bodies [37]. In his analysis he derived from elasticity equations an expression for the tangential compliance when a tangential force was applied in a quasi-static way. He showed that as small as the tangential traction may be, "micro-slip" will occur at the boundary of the contact region and spread inward if the traction is increased until "gross-slip" is established. This led him to describe the partition of the contact surface into stick and slip regions. This was further extended to various cases of loading and unloading [38]. Mindlin stressed the fact that the changes in tractions and displacements during contact depended not only upon the initial state of loading but upon the entire history of loading and upon the instantaneous rates of change of the normal and tangential forces.

About 25 years later, taking advantage of the understanding provided by Mindlin, Maw et al. [39] proposed a theoretical solution to stress and displacement fields during an oblique collision through numerical integration of the contact forces. They showed that according to the pre-collision velocities, three types of collisional behaviors were to be expected: for small incidence angles, i.e. quasi-normal contact, the contact surface includes a central disk where the particle stick together, while at larger values "gross-slip" [37] persists throughout the contact. At intermediate values however initial gross-slip may be interrupted by the friction force and therefore the particles will eventually stick until separation. They also showed that the problem could be formulated in terms of a single dimensionless angle of incidence which will be illustrated in Chapter 3. With this analysis, although the coefficient of restitution was implicitly taken to be unity (as in Hertz's theory), they showed that under suitable

circumstances the elastic energy stored during the loading phase of the contact is recoverable and the velocity of the contact point in the tangential direction [1] may reverse. This "superball" effect [40] is not predicted by the classical theory of impact of two rigid bodies based on the conservation of energy and momentum. Their theoretical prediction was reproduced experimentally by following the trajectories of an air table puck cut from a sphere and bouncing off a flat surface [41] and surface velocity reversal was evidenced over a significant range of incidence angles.

2.3 Macroscopic Model of Impact

Unfortunately it is impossible to incorporate all the details of Maw et al.'s analysis either in theories or numerical simulations because both require that a numerically and analytically simple collision model be available. On the other hand, whatever the approximate modelization of a binary impact may be, there are some features that it should be able to account for: e.g., the tangential effects which can greatly affect the outcome of a collision as evidenced by Maw et al. and energy losses during collision. These losses can occur in many forms: initial kinematic energy either transferred or lost as elastic strain energy, friction, plastic strain energy, fracture, light, sound and so forth. Due to the complexity of the foregoing mechanisms the impact of two frictional inelastic particles is best described in terms of phenomenological quantities.

2.3.1 Collision Properties of Inelastic Frictional Spheres

The Coefficient of Restitution: For head-on collisions the dissipation effects are described by a coefficient of restitution e. It is usually defined as the ratio of the normal component of the relative velocity of the two impacting bodies just after collision to that just before. Other definitions are possible which are not strictly equivalent in some cases [42]. Throughout this thesis we will use the above mentioned

---

[1]The tangential velocity which we will also refer to as the surface velocity as defined in Chapter 3 is the relative velocity of the contact points of the bodies.

kinetic definition. It has been known for about a century that e is not a material property in as much as it actually depends on the magnitude of the impact velocity [43] and is further likely to be affected, especially at minimal impact velocities, by other effects such as those produced by the polish of the surface of the colliding bodies [44]. According to Kuwabara et al. [45], the mechanisms responsible for energy dissipation in such collisions are of three kinds [45]:

1. viscosity of the materials damping the elastic deformation,

2. plastic flow for velocities higher than a yield velocity and fracture,

3. vibrations of the spheres caused by impact and remaining in each sphere after a collision.

Most of the experimental data available on this topic [43] refers to impacts of a sphere on a fixed (flat) target. For colliding spheres it has been shown [34] that the third mechanism could be neglected for pratical speeds (1-10 m/s) and would anyway be preempted by other mechanisms for values of speed lower than those above which this assumption would fail. Independantly of geometrical factors, e is expected to take values close to unity for low impact velocities and to decrease with increasing normal velocity magnitudes. For example, the early observations of Raman [44] using two metallic spheres hung by bifilar suspensions and impinging at low velocities (from a fraction of to a hundred cm/s) corroborated this expectation. Other experiments reported in Ref. [43] show similar behaviors.

The first mechanism above has been studied as an improvement upon Hertz's theory by Kuwabara et al. in [45]. This led to the prediction that the decrease of e would be given by $(1 - e) \propto (impact\ velocity)^{\frac{1}{5}}$. They carried out an experiment similar to that done by Raman by colliding two pendula. Although the agreement seems satisfactory for materials with high coefficient of restitution (steel, brass, glass), it is not clear how well the decrease of e compares with a 1/5 power of

the velocity. The second mechanism was studied independently by Ning et al. [46] and Johnson [40] who found e to be proportional to $(impact\ velocity)^{-\frac{1}{4}}$, an expression which has proved to agree qualitatively with some experimental observations. However, experimental results of spheres impacting flat targets reported by Johnson [40] and borrowed from Ref. [43] show almost perfect agreement. As mentioned in [45], for a material where this mechanism predominates, the coefficient of restitution should remain close to unity until yield occurs and sharply decrease for higher velocities. It is therefore qualitatively very different from the first mechanism where e is expected to decrease sharply from zero impact velocities, which is more likely to occur for materials like hard metals or plastic where visco-elastic effects predominate at small deformations [45]. It is worthwhile noticing in both cases that the predicted decay of e is slow which somewhat justifies the use of an "average" value of e for a given order of magnitude of the expected impact velocities. Finally each model predicts a different size dependance for the coefficient of restitution, an issue about which very little experimental work has been done so far. Although some experimental results reported in [43] seem to indicate a slight decrease of e with the size of two impacting spheres , other results from [43] show no variation of e when the size ratio of the two impinging spheres is varied from 1 to 15.

Friction and Surface Velocity Reversal: Friction is another cause of energy dissipation. The original concept of solid friction may be extended to the case of impacting bodies and defined as the ratio μ of tangential to normal impulse exerted by one body on the other when they slide on each other throughout the impact. In this case μ takes it dynamical value μ_d, which may differ from the static value obtained to initiate a sliding motion. Experiments reported by Brach [47] of spheres impacting thick plates show that μ does reach a constant value for large incidence angles of the spheres. Other results however show examples of impacts accompanied by surface indentation for which μ tends to decrease at higher angles of incidence.

When sliding does not last throughout the impact: i.e., when it is damped by a large enough frictional force, Coulomb's law is not applicable. However, while the classical theory of rigid bodies would predict that the two bodies are subsequently "rolling" with no tangential velocity at separation, Maw et al. [39] showed that the relative surface velocity could go through zero and reverse because elastic strain energy is restored and maintains the contact surfaces in relative motion. Because real surfaces are rough, the surface velocity restitution is usually incomplete and may be characterized by a tangential coefficient of restitution as will be seen in section 2.3.2.

2.3.2 Collision Operators

In kinetic theories, macroscopic quantities are derived by averaging a given velocity distribution function over all the collisions. For pratical purposes, the latter are modeled through a "collision operator" relating pre- and post-collision relative velocity components through phenomenological quantities. The simplest form of collision operator for dissipative collisions of particulates uses only the coefficient of restitution in the normal direction. Tangential effects are not always accounted for in order to keep the different integrations tractable. In an effort to take surface roughness into account , Jenkins et al. [48] and Lun et al. [49] introduced a constant coefficient of tangential restitution β analogous to that acting in the normal direction. For real particles β is not constant, but varies between the theoretical limits of -1 and +1, depending on the material properties and the geometry of the collision. To account for "sliding" collisions Jenkins, [50] introduced a constant coefficient of friction relating the normal and tangential impulses. Finally Lun and Savage [51] used an impact velocity dependent coefficient of restitution.

A more complete collision operator was proposed by Walton [52]. This operator consists of:

- the coefficient of restitution e in the normal direction

- a tangential coefficient of restitution β

- a coefficient of sliding friction, μ

In his model any collision is either "sliding" or "rolling" and tangential effects (i.e. decrease and reversal of the tangential velocity of the contact point) are readily included by making β a function of the incidence angle taking values between -1 and a positive constant β_0. Obviously, the physical meaning of β_0 is not straightforward. It imposes a maximum restitution of the tangential velocity when the latter is reversed. We will discuss this operator in more detail in section 3.2.

2.3.3 Computer Simulations

While "event-driven" type of simulations make use of collision operators, the forces models prescribed in MD approaches are not so straightforward. Some of them readily allow reversal of tangential surface velocity [18, 45, 52, 53]. But no explicit assumption is usually made about the coefficients of restitution in the normal and tangential directions. Recently, Schafer et al. [54] carried out a thorough testing of each of them and showed that with an adequate value of the normal to tangential stiffness ratio, Maw et al.'s data taken as a basis for comparison was closely reproduced by these force schemes. However the variation of the normal coefficient of restitution with the initial normal relative velocity they produce is rarely close to experimental observations except for the Hertz-Kuwabara visco-elastic force scheme [45] and the normal force model proposed in [18] where two different spring constants are used for loading and unloading in an attempt to mimic plastic deformation effects. On the other hand Ning et al. [46], in order to test their theory used a modified version of TRUBAL were plastic effects where explicitly included as a modification of Hertz's law for pressures exceeding the yield pressure and thus qualitatively reproduced their prediction. Incidentally, the force model of

[18] predicts a dependence of e on the magnitude of the impact velocity at least qualitatively very similar to that obtained numerically by Ning et al. [46].

Finally, as mentioned in [54] the reduced mass of the two colliding spheres is sometimes included and sometimes not as a prefactor in the damping part or the elastic part of these forces, sometimes in both. This makes the coefficient of normal restitution a different function of this reduced mass in each case. Experimental verification of this dependence is therefore very important.

2.4 Other Experimental Observations

2.4.1 Collision Properties of Spheres

Experimental data on collision properties are scarce. In order to test their theory, Maw et al. [41] performed, as mentioned earlier, a two-dimensional study that followed the trajectory of a puck gliding on an air table and bounced off a flat plane. They observed the predicted reversal of the relative tangential velocity and also measured a very stable coefficient of dynamic friction.

Non intrusive video techniques have been further developed to measure translational and rotational velocities of two-dimensional assemblies of grains or to investigate collisional properties of spheres. Foerster et al. [55], used a video camera to record the motion of two colliding spheres (either glass or acetate) being dropped with no initial velocities and no spin in a vertical plane. Due to the absence of spin prior to collision, its measurement after collision is redundant. They find a good agreement of their data with both Maw et al.'s theory and Walton's model. In the case of the impact on a plate, the transition from gross-slip to collisions involving sticking is not precisely captured by this operator. They also note that Maw et al.'s theory is more successful for similar materials. However, the apparatus used did not allow Foerster et al. to scan a wide enough range of relative velocity so as to observe

the influence of the normal velocity at impact on the coefficient of restitution e or that of the tangential velocity on the other parameters.

Sondergaard et al. [56] carried out a thorough study of the impact of a sphere with zero initial spin on a flat plate. Although their work was more focused on the influence of the plate supports and on the ratio of the sphere diameter to the thickness of the plate, it is interesting to note that their results show a slight but systematic increase of e with the angle of incidence. They also found that they could reduce, but not eliminate, the scatter obtained on the values of their tangential coefficient of restitution [2] , but not eliminated, by carefully cleaning the surfaces with acetone prior to collision. This influence of the effective frictional conditions near the point of impact is more important for glancing collisions.

Dave et al. [57] developed an experiment allowing them to evaluate collision properties of nylon spheres using high speed video analysis and, for the first time, an apparatus where the incident trajectories lay in the same plane but were otherwise arbitrary. Their results showed good agreement with Maw et al.'s theory and substantiate the simple impact model due to Walton. However this work was focused on the feasibility of such an experiment and it is not clear how they computed the coefficient of restitution and for what range of impact velocities their results were obtained. The topic of this thesis is closely related to the latter work, and further details will be given in the following chapters.

2.4.2 Image Analysis and Granular Flows

Finally we would like to draw attention on the variety of imaging methods which have been used in the study of granular materials with different purposes. Drake et al. [58, 59] performed two-dimensional inclined chute flow experiments in which quantitative information was obtained by employing a combined procedure of manually digitizing

---

[2]The tangential coefficient of restitution used here does not include rotational velocities but describes only the motion of the center of mass of the sphere.

frames together with the use of software to compute particle velocities and spins between collisions. Reduction of the data was confounded due to the interference of the walls [60] and it is not certain whether collisional properties can be inferred from such an analysis.

Ahn [61] used fibre-optics pointed through a lucite sidewall to measure the downstream components of the mean velocity, the velocity fluctuation and the linear particle spacing of glass beads flowing in an inclined aluminum chute.

Recently Warr et al. [62, 63] used a high-speed camera and a Hough Transform-based software to derive from the motion of the spheres distributions of velocity and density profiles in a two-dimensional vibrated bed. But this experiment was not focused on collisional properties. Finally the development of NMR imaging methods for granular flows is perhaps one of the most promising nonintrusive imaging techniques.

2.5 Conclusion and Motivation

Interpretation of physical experiments and validation of computer simulations and theoretical modeling of rapid granular flows require a knowledge of the properties of the flow materials used in experiments which makes it necessary to design a three-dimensional experimental technique to allow for the most arbitrary conditions of impact. These experiments should not be limited to the determination of three collision properties, but should also include as much as possible their dependance, if any, on the magnitude of the normal and tangential velocities of approach. To observe such a dependence it is necessary to scan a large interval of impact velocity magnitudes. Finally, the relation of these properties with the particle sizes is still to be investigated. The purpose of this work is to present such experimental results using an experimental setup similar to and as simple as that used in [57].

CHAPTER 3

THEORETICAL PREDICTIONS

3.1 Introduction

The collisional properties we want to measure are phenomenological constants which are able to describe the changes in momentum, both linear and angular, of two colliding inelastic frictional spheres. This is done by comparing our experimental measurements with a simple impact model proposed by Walton. The results of interest to us are presented here and a more complete derivation is given in appendix A.

3.2 Walton's Collision Operator

Let us consider two homogeneous (see Figure 3.1) spheres with masses m_1 and m_2, diameters σ_1 and σ_2, moments of inertia about their center I_1 and I_2 ($I_i = m_i \sigma_i^2 / 10$) and colliding when there centers lie at $\vec{r}_1$ and $\vec{r}_2$. Prior to the collision the center of the spheres have velocities $\vec{v}_1$ and $\vec{v}_2$ and the spheres are spinning with rotation vectors $\vec{\omega}_1$ and $\vec{\omega}_2$. Because the spheres exert an impulse on each other during the collision these quantities are changed when they separate. The new values of velocities and rotation, hereafter denoted with a prime, are obtained from the conservation of linear and angular momenta and prescribed relations using the collisional properties.

$\vec{n} = (\vec{r}_1 - \vec{r}_2)/|\vec{r}_1 - \vec{r}_2|$ is the unit vector joining the centers of the two spheres. The relative velocity of the spheres at their contact point, or sliding velocity, before collision is (see Figure 3.2):

$$\vec{v}_c = \vec{v}_1 - \vec{v}_2 - \left(\frac{\sigma_1}{2}\vec{\omega}_1 + \frac{\sigma 2}{2}\vec{\omega}_2\right) \times \vec{n} \tag{3.1}$$

This velocity has a normal component $\vec{v}_n = (\vec{v}_c \cdot \vec{n})\vec{n}$ and a component lying in the

15
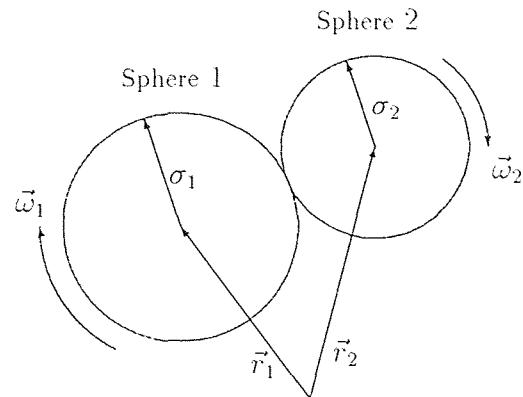
Figure 3.1 Colliding spheres with spins.
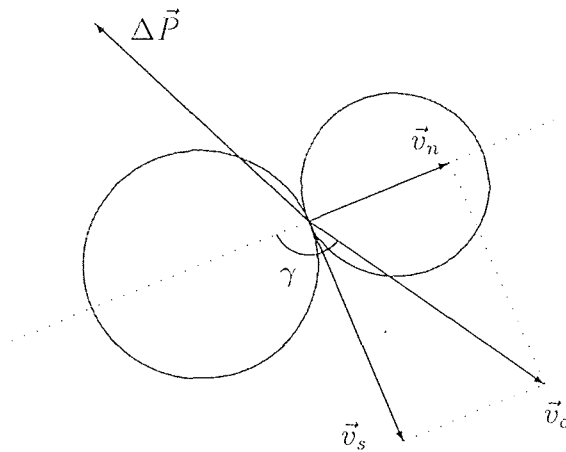
Figure 3.2 Relative motion of the two spheres of Figure 3.1 and impulse $\Delta \vec{P}$ exerted by sphere 2 on sphere 1.

tangential plane $\vec{v}_s = \vec{v}_c - \vec{v}_n$. The normal coefficient of restitution is defined as:

$$(\vec{v}_1' - \vec{v}_2') \cdot \vec{n} \overset{def}{=} -e\,(\vec{v}_1 - \vec{v}_2) \cdot \vec{n} \tag{3.2}$$

while the coefficient of tangential or rotational restitution is:

$$\vec{v}_s' \overset{def}{=} -\beta\,\vec{v}_s \tag{3.3}$$

Possible theoretical values of β lie in the interval $[-1;1]$. As mentioned earlier (Chapter 2), for tangential effects to be taken into account, β has to be a function of the angle of incidence γ [1] . This dependence, as predicted by Walton's model is shown in Figure 3.3. In order to determine the tangential component of momentum change, Walton assumes that a given collision is either *sliding* or *rolling* throughout the contact. In the first case, the tangential component is set equal to its frictional limit according to Coulomb's law: its magnitude is a coefficient of friction μ_0 times the magnitude of the normal component and it is parallel, but oriented in the opposite direction, to the tangential component of the contact velocity. Since Coulomb's law applies only to sliding and could otherwise lead to an increase of energy for small angles of incidence (see Appendix A), i.e. nearly head-on collisions, rolling is effective whenever for a given collision the sliding assumption yields a β value greater than β_0, an apriori unknown positive constant smaller than one as shown in Figure 3.3. Along with e and μ_0, β_0 becomes the third unknown collision property we wish to determine from our experiment. The equations relating the pre- and post-collisional kinematics of the spheres are given by Walton [52]:

For sliding:

$$-\frac{v_s'}{v_n} = -\frac{v_s}{v_n} - \mu_0 (1 + \frac{1}{K})(1 + e) \tag{3.4}$$

For rolling:

$$\frac{v_s'}{v_n} = -\beta_0 \frac{v_s}{v_n} \tag{3.5}$$

---

[1]γ is shown in Figure 3.2; it is such that $\cot \gamma = v_n / v_s$.
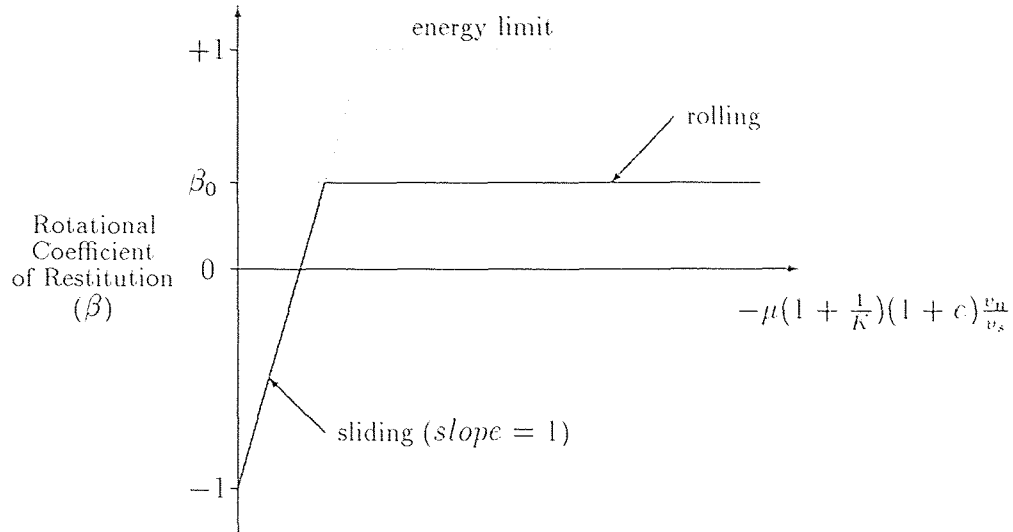
Figure 3.3 Variation of the coefficient of tangential restitution with the angle of incidence as given by equation A.10.

Where $K = \frac{4I}{m\sigma^2}$ is a constant equal to $2/5$ for homogeneous spheres. The illustration of these equations is given in Figure 3.4. The analysis of a single collision yields the coefficient of normal restitution and only one of the two other parameters β_0 and μ_0. Indeed for a sliding contact, β is a function of the angle of approach while μ_0 is now given by the ratio of the tangential to the normal component [2] of the impulse $\Delta\vec{P}$. On the other hand, when rolling prevails β is equal to β_0 but f is now varying. Although it is not known apriori whether a particular collision will be "rolling" or "sliding", it is still possible, according to Walton's model, to determine μ_0 and β_0 by producing a plot of v_s'/v_n values versus v_s/v_n values. β_0 is given by the slope of the straight line describing rolling while the y-intersect of the other line yields $-\mu_0(1 + \frac{1}{K})(1 + e)$.

It should be noted that the above equations remain valid for an arbitrary function β of the incidence angle or a non constant coefficient of restitution. Without

---

[2] We shall hereafter refer to this ratio as the *impulse ratio* and call it f.
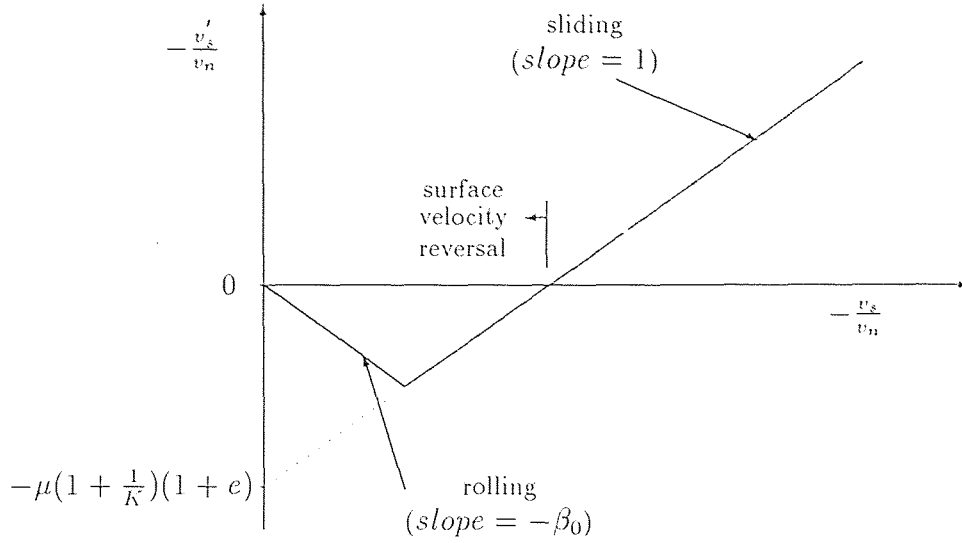
Figure 3.4 Relation between the tangents of the recoil and incidence angles in the *sliding* and *rolling* regimes as predicted by equations 3.4 and 3.5 from Walton's collision operator.

assuming any particular form of the functions β or f, the impulse ratio and the angle of incidence γ, they are still related according to the above model as follows:

$$\beta(\gamma) = -1 - (1 + \frac{1}{K})(1 + e)f(\gamma)\cot\gamma \tag{3.6}$$

This follows from the fact that one of the basic assumptions made in this model is that their is no torsional reaction between the spheres, so that the direction of the relative tangential velocity is unaltered. On the other hand while the computation of v_s before collision requires the knowledge of the spin of the spheres, that of v_s' and thus of β may be done alternatively from equation A.4. without any knowledge of the spins after rotation.

CHAPTER 4

EXPERIMENTAL METHOD

4.1 Introduction

Our intention is to track the motion of two colliding identical spheres in free fall under gravity using a single imager. The only experiment we know of, involving two spheres colliding in such conditions, is that presented in [55] and referred to in Chapter 2. In this experiment, the spheres where allowed to collide in a very limited range of relative velocities ($1.18 \pm 0.06\,m.s^{-1}$) with adjustable orientation and no initial spin. This restriction allowed the authors to avoid the computation of spin before and after collision as was explained at the end of Chapter 3. The experimental apparatus used here is designed to produce a much wider range of relative velocities but does not allow any control of the inital spin imparted to the spheres, and therefore requires that the rotations be computable with sufficient accuracy. The collisions are recorded with a single imager and the positions of the individual spheres are tracked from frame to frame. The spin may be inverted from the motion of black dots imprinted on the surface of the spheres.

4.2 Experimental Apparatus and Procedure

The apparatus is essentially the same as that described in [57, 65] except for a few modifications. It consists of two horizontal cylindrical aluminum tubes, the axes of which lie in the same vertical plane. Each of them is mounted on a micro-positionning slide, one for horizontal translation and the other for vertical translation.

The inner diameter of the tubes is just a little larger than the diameter of the sphere it holds. Different tubes may be mounted with different inner diameters allowing the use of different sphere sizes. One end of each tube is plugged into a pressurized air supply, while a vacuum pump is used to hold the spheres in place. A single sphere is placed at this end of each tube which is expelled with a velocity

20
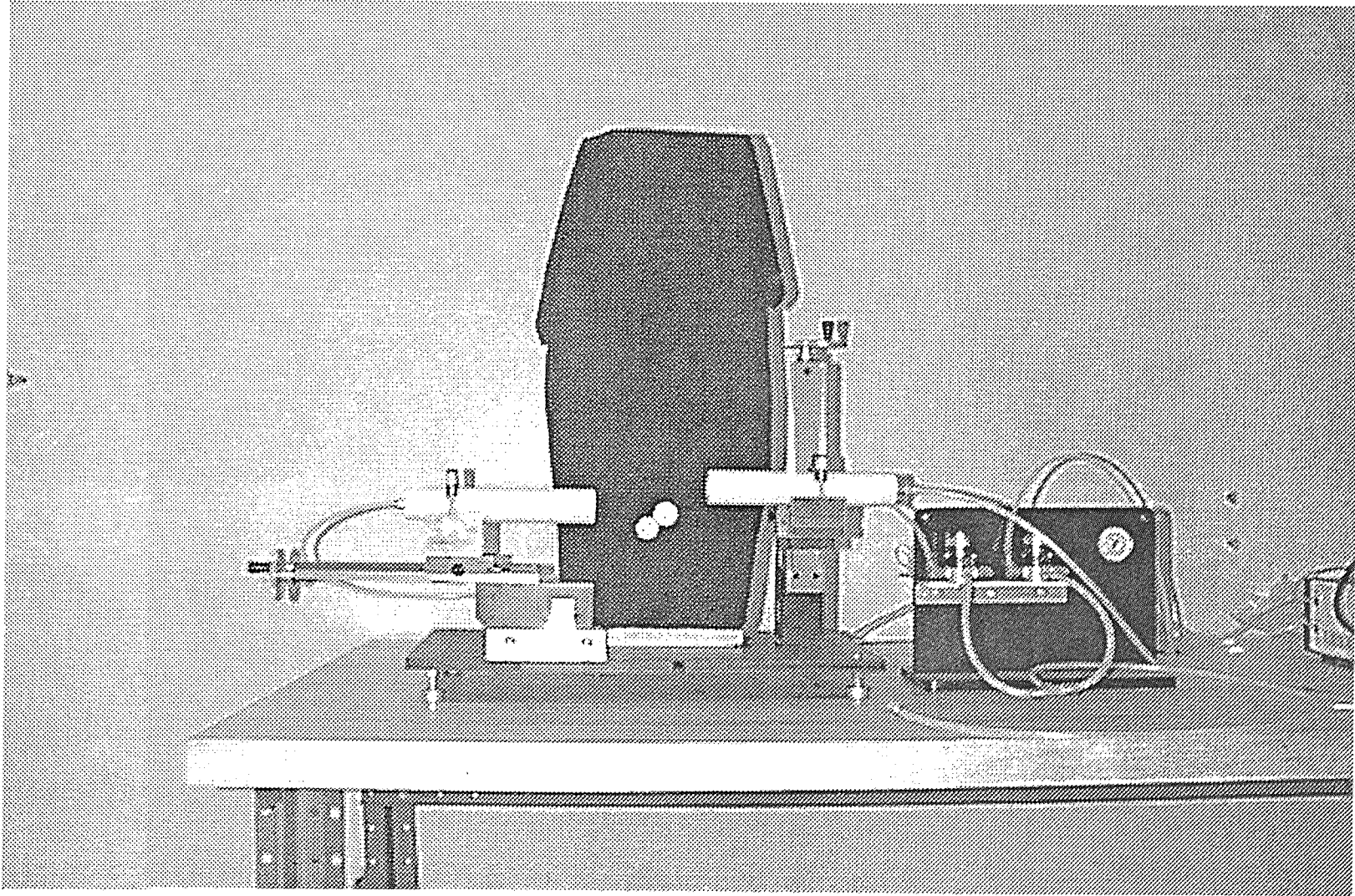
Figure 4.1 Experimental Apparatus
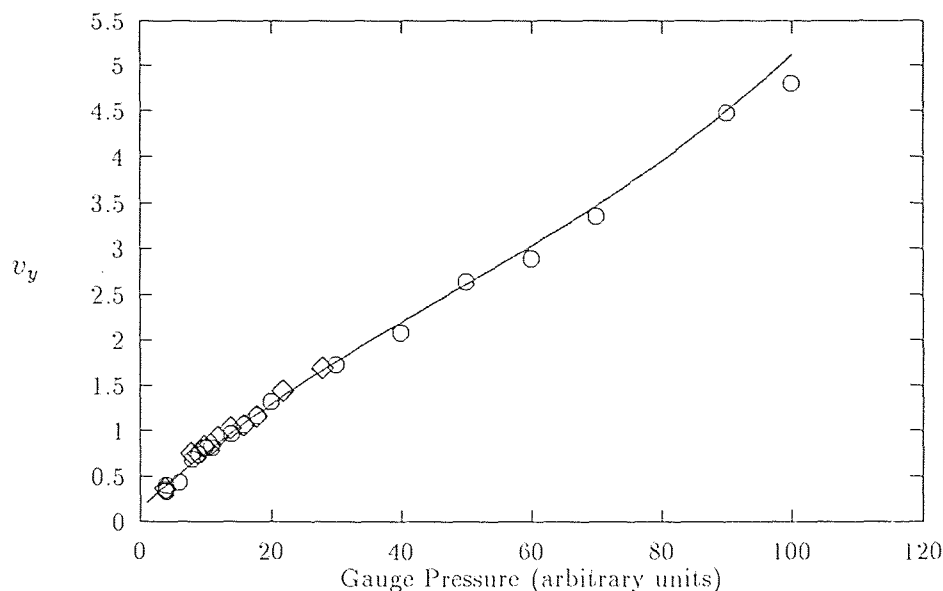
Figure 4.2 Average exit velocity (expressed in meters per second) of the spheres versus reading of the pressure gauge for 2.54 cm diameter Nylon ($\Diamond$) and Teflon (o) spheres. The solid line is a least-squared cubic fit providing approximate prediction of this data given by: $v_y = 0.143 + 6.6(\frac{p}{100}) - 5(\frac{p}{100})^2 + 3.38(\frac{p}{100})^3$

depending on the imposed pressure. Figure 4.2 shows measurements of exit velocities in meters per second versus values of the imposed pressure for two types of 2.54 cm diameter spheres. Since the mass ratio of the two spheres was about 1.8, the collapse of this data on a single line shows that the tubes are long enough so that the spheres exit with the velocity of the air jet which is important as far as repeatability of the experiment is concerned. Relative impact velocities can be varied up to about $10\,m.s^{-1}$. In order to check the alignment of the tubes in a vertical plane, a piece of carbon paper was placed on the end of a tube and a sphere was launched from the other one. After coming out of this tube, the sphere travels a distance of the order of 30 cm, before it hits the carbon paper target upon which it imprints the location of the impact. This experiment is repeated twenty times. The target is then placed upon the other tube and the experiment is performed again the other way round. The maximum horizontal offset of the impact point relative to the vertical symmetry

axis of the inner section of the target tube was one millimeter on both sides of the axis, for both shooting directions. This means that the maximum off-plane velocity component will be less than one percent of the other components. However there is still the possibility that angular momentum is transferred to the spheres. Therefore this setup is intrinsically three-dimensional. However if the in-plane components of the spins are small enough so that their contribution to the tangential velocity may be neglected, the motion of the spheres remain two-dimensional. Although as suggested by Dave et al. [57], it is in principle possible to obtain on the same image a front view and a top view of the spheres by using a 45° inclined mirror reflecting the top view within the view field of the imager we did not use this technique (because it considerably reduces the scaling between the image space and the physical space, i.e. the resolution of the images). Instead the out-of-plane translational velocities were determined from the computed rotation vectors. This point will be discussed in Chapter 5.

The collision takes place between the tubes in a plane parallel to the focal plane of a Kodak Ekta Pro 1000 high-speed video camera recording at a rate of 1000 frames per second. By using the positioning slides, any geometrical angle of incidence may be obtained. The procedure consists of launching the spheres with the pressurized air and recording the collision at a rate of 1000 frames per second with the high speed camera. A 90mm Nikon objective is used for 2.54 cm spheres and a 200mm Nikon objective is employed for smaller sizes. We use double front lighting on a black background with 750 Watts Lowell DP lamps. An image intensifier is necessary. The gate period (i.e. the time the diaphragm remains open) may be adjusted between 10 μsec and 5 $msec$ according to the velocity of the spheres to avoid blurring. Recording is triggered manually. The resulting gray level images are then replayed on a monitor. All the images for which both spheres lie entirely in the field of view are saved and downloaded to a PC using an interactive software

[66]. The number of such images varies between 4 and 20 according to the size of the spheres and the impulse which they are initially given. Finally, these images are downloaded to a UNIX platform for processing. The subsequent analysis is detailed in Section 4.4. Figure 4.2 shows a sequence of such gray level images.

4.3 The Spheres

The spheres we used in this experiment were made of white plastic materials: Nylon 6/6 or Teflon. We used $2.54cm$ diameter spheres for both materials and experimented on $1.27cm$ diameter nylon spheres as well. On the surface of each of them, black dots were imprinted with either a permanent black marker for Nylon or black enamel paint for Teflon spheres. These black markers have linear dimensions of the order of ten times smaller than that of the spheres The fraction of the surface area of the spheres covered by these dots is about 5% thus limiting the probability for the contact area during impact to overlap with one such dot to a marginal value.

4.4 Image Analysis

As mentionned by Dave et al. [57] the main difficulty of the experiment was initially the ability to obtain good accuracy on the spheres and markers positions in space with a low resolution imager (192×239). The image analysis software we used was originally the result of different contributions made in our laboratory during the past years [65, 67, 68] but was substantially modified. The ultimate task of this software is to determine the evolution of the relative positions of the spheres and the location of the dots on the sphere surfaces with sufficient accuracy, starting from 192×239 gray level images recorded 1ms or more apart from each other (see Section 4.2). This is performed first by an *edge detection* phase, where the contours of the two spheres and those of the imprinted black dots are marked after the initial gray level image has been reduced to a binary image. Following this, a *clustering* algorithm is used

t=0

t=2

t=4

t=5

t=6

t=7

t=8

t=10
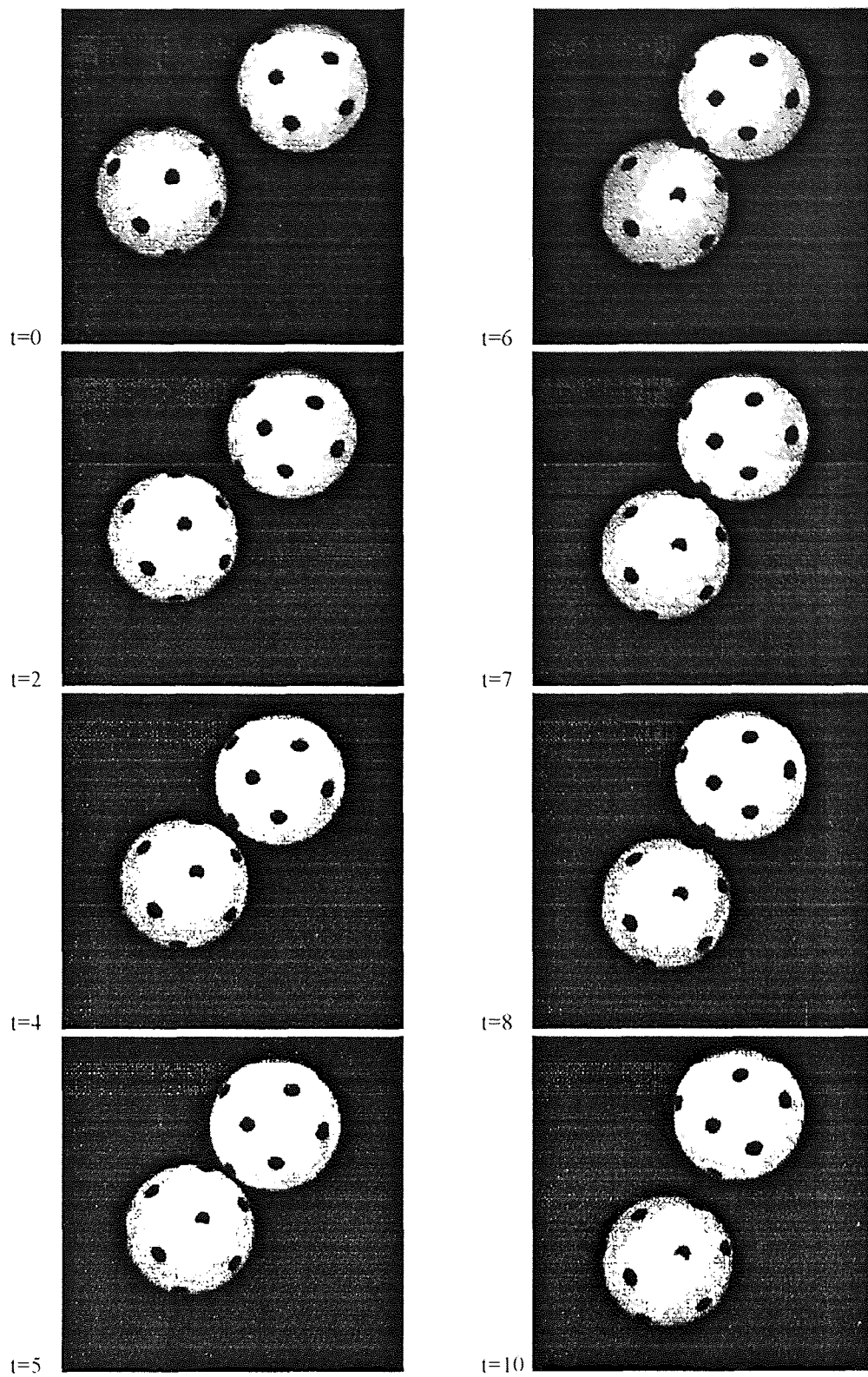
Figure 4.3 Sequence of collision images. The time t is indicated in ms at the lower left corner of each frame. The collision takes place between $t = 8$ and $t = 9\,ms$.

to fit ellipses and circles on the edge points. Here an Adaptative Hough Transform algorithm is used to find the circular contours of the spheres as described in Section 4.4.2 and a different "matching" algorithm is used (see Section 4.4.3).

4.4.1 Edge Detection

The complete edge detection algorithm is described in [69]: The "Laplacian of Gaussian" or LoG, is used with a standard deviation or space constant of 2. The choice of this constant depends on the size of the markers compared with that of the spheres and the signal-to-noise ratio. The resulting convolution mask is a 17×17 grid. Because in some cases the displacement of a sphere on the 192×240 pixel grid of the camera can be close to a pixel, subpixel accuracy is used and is implemented as also described in [69]. First zero-crossings of the initial LoG image are detected. Here the LoG images are converted in integers rescaled between -1000 and +1000. The search for zero-crossings uses a set of predicates [69] where a zero-crossing is marked at the location given by one of the predicates if the latter matches a 3×3 local neighborhood in the image. We use a threshold value of 20 below which a given pixel is considered equal to zero. These values are chosen empirically in order to eliminate most of the remaining noise pixels while preserving actual edges. A set of Tchebychev polynomials is fit onto the 3×3 neighborhood of each zero-crossing of the LoG image. This neighborhood is then refined by interpolation of these polynomials into a 12×12 subpixel neighborhood. The zero-crossings of this subdivided neighborhood are the final edge points we keep. Preliminary precision tests concerning the subpixel technique have been carried out and were reported in [65]. Finally, a labelling algorithm assigns a different integer value to each group of connected pixels. The reason for performing this labelling is explained in the following section.

4.4.2 Adaptative Hough Transform and Fuzzy-Clustering Algorithm

Once the edge points have been determined, it is necessary to identify the resulting shapes as being the contours of the black dots (approximately elliptical) or those of the spheres. This is done with the "Adaptative Hough Transform" technique [70] for the sphere contours. An accumulator array of $30 \times 30 \times 15$ (the smallest dimension corresponds to the initial resolution on the radius) is used. This array initially maps the entire image. AHT iterations are performed until the maximum distance covered by one array element is less than 0.5 pixel. An "Adaptative Noise Fuzzy-Clustering" [71, 72, 73, 74, 75] algorithm is used as in [57] to find the position of the markers' centers in the two-dimensional plane of the image by fitting ellipses on their contour. The value of the noise multiplier, λ, defined in [72] is taken to be 1. The markers are then reduced to the centers of the ellipses only. One advantage of the Hough Transform technique over the fuzzy-clustering technique used in [57] is that the number of objects does not need to be specified as an input variable. Therefore even though the sphere contours may sometimes be segmented due to locally poor contrast conditions, thus yielding more clusters than actual edges, labelled clusters belonging to these contours can be separated from those belonging to the contours of the dots after performing the Hough Transform. To do this, we first define for each sphere, an annulus concentric with the circle detected by AHT. The outer and inner diameters of this annulus are taken as the detected radius respectively plus and minus a fraction of this radius. Then clusters are considered as being part of the sphere contour if one half or more of the points they contain lie inside this annulus. A percentage of 4% of the radius is used. The remaining clusters are either noise or dots contours. Since in our images each of the latter is always contained in a single cluster, the fuzzy-clustering technique may now be applied. At this point, if a noise cluster is still present its size is small enough compared to the others so that it can easily be recognized and removed.

4.4.3 The Matching Algorithm

Up to this point each of the six initial frames has been analyzed independently and for each, the positions and geometries of the spheres and markers have been determined. It is necessary to match from each frame to the next clusters produced by the same marker or the same sphere. A sphere in one frame is matched to the closest sphere in the next frame. For the markers more caution has to be taken. The simple technique based on the assumption that displacements from one frame to the next are small is rejected as being too restrictive. An alternative is to try to match markers by groups of three with the constraints that the triangle that their centers form be not deformed and keep the same orientation. This solution turned out to be unsatisfactory because a maximum deformation had to be imposed which depended very much on the quality of the image but also on each collision. It was retained though as we will see as a speed-up technique. Matching of the markers is done for the frames before and after collision independently for each sphere by using three frames at a time. We first define a direct orthonormal coordinate system (x, y, z), the x and y axes lying in the plane of the image and z pointing towards the observer. This coordinate system does not change with time. The center of one of the spheres, say sphere a, in frame p is located at X_0^p with components x_0^p, y_0^p, the z-component being zero. The jth dot is located at X_j^p with components x_j^p, y_j^p, z_j^p. Another coordinate system whose center is the center of sphere a and same axes as the previous one is defined in which the three dimensional relative position of the jth dot in frame p is given by: $\tilde{X}_j^p = X_j^p - X_0^p$. The z-component of $\tilde{X}_j^p$ is computed as:

$$\tilde{z}_j^p = z_j^p = \sqrt{R^2 - |\tilde{x}_j^p|^2 - |\tilde{y}_j^p|^2} \tag{4.1}$$

For each triplet of dots i, j, k in frame p we define the three vectors:

$$a_{ijk}^p = \tilde{X}_i^p - \tilde{X}_j^p$$
$$b_{ijk}^p = \tilde{X}_j^p - \tilde{X}_k^p \tag{4.2}$$

$$c^p_{ijk} = \dot{X}^p_k - \dot{X}^p_i$$

which are the three sides of the triangle formed by the triplet of dots (i, j, k) in frame p. For any dot triplets, (i_p, j_p, k_p), (i_q, j_q, k_q), (i_r, j_r, k_r), belonging respectively to three consecutive frames p, q, r, we define the matching function over three frames p, q and r for these three triplets as:

$$
\begin{aligned}
\mathcal{M} &= \left(\Delta_{qr} a^p_{i_p j_p k_p} - (\Delta_{pq} + \Delta_{qr}) * a^q_{i_q j_q k_q} + \Delta_{pq} a^r_{i_r j_r k_r} \right)^2 \\
&+ \left(\Delta_{qr} b^p_{i_p j_p k_p} - (\Delta_{pq} + \Delta_{qr}) * b^q_{i_q j_q k_q} + \Delta_{pq} b^r_{i_r j_r k_r} \right)^2 \qquad (4.3) \\
&+ \left(\Delta_{qr} c^p_{i_p j_p k_p} - (\Delta_{pq} + \Delta_{qr}) * c^q_{i_q j_q k_q} + \Delta_{pq} c^r_{i_r j_r k_r} \right)^2
\end{aligned}
$$

where Δ_{mn} is the time interval between frames m and n. In each of the three consecutive frames p, q, r, we now pick one dot triplet, which we call respectively (i_p, j_p, k_p), (i_q, j_q, k_q), (i_r, j_r, k_r). respectively, as: It has been found that minimization of $\mathcal{M}$ with respect to the choice of triplets (i, j, k) provided the right matching. More precisely if one triplet is chosen in frame p, $\mathcal{M}$ is minimized when the two triplets picked in frames q and r are those obtained by successive rotation of the inital triplet in frame p, with the same rotation vector as that of the sphere. However, if the position of a sphere center is not properly determined by the clustering algorithm, the matching may also turn out to be erroneous. This function can be reduced to matching two consecutive images only by setting to zero the part of it pertaining to the third frame (frame r in the example above). This alternative is required when only two frames are available either before or after collision. The matching is performed on each group of three consecutive frames but the resulting matching for the first two frames of each group only is conserved except for the last group of three frames where we need the correspondence between the last two frames. Since the minization of $\mathcal{M}$ over three frames requires testing many marker triplets, the choice of these triplets is reduced by considering the area of the triangle they form: three triplets of markers (one in each frame) are candidates for matching

under the condition that the relative change in the area of the triangles they form is less than 10% and their orientation is conserved. In our algorithm we also added the constraint that the dot product of two sides of this triangle should not vary more than 10%.

CHAPTER 5

RESULTS AND DISCUSSION

5.1 Computation of Translational and Rotational Velocities

5.1.1 Translational Motion in the Focal Plane

As explained in Chapter 4, the trajectories are obtained from the analysis of individual gray level images. The edge detection techniques successfully make out the features of these images that are the boundaries of the spheres and those of their markers. Figure 5.1 shows an example of gray level image and corresponding edge image below with the circles best fitting the sphere boundaries and the centers of the detected clusters. In order to obtain the velocities and positions of the spheres at the moment of collision, we perform a least-squares second degree polynomial fit of the positions of the center of the spheres extracted from each edge image as shown in the above example, independently before and after collision. This is based on the assumption that, while in free flight, the two spheres are subject to a constant acceleration. Figure 5.2 shows the trajectories of the centers of two colliding spheres before and after collision. Six images before the collision and six after where recorded. In this experiment, the collision takes place between frames 6 and 7 which are the frames immediately before and after collision. The circles are the position of their centers determined according to the method presented in Chapter 4 while the four solid lines are the four second degree least-squares fits performed for each sphere before and after collision independently. The axes are graduated in units of sphere diameter and the number of subpixels per diameter is approximately 255. We find that the maximum standard deviation of the distance of the center positions to the parabolic fit both in the x and y directions, are of the same order: $\sigma_x \simeq \sigma_y \simeq 1.5$ in subpixel units. By computing the components of the average velocity of the sphere centers between two consecutive frames, we also determine the standard deviation of these velocity measurements with respect to
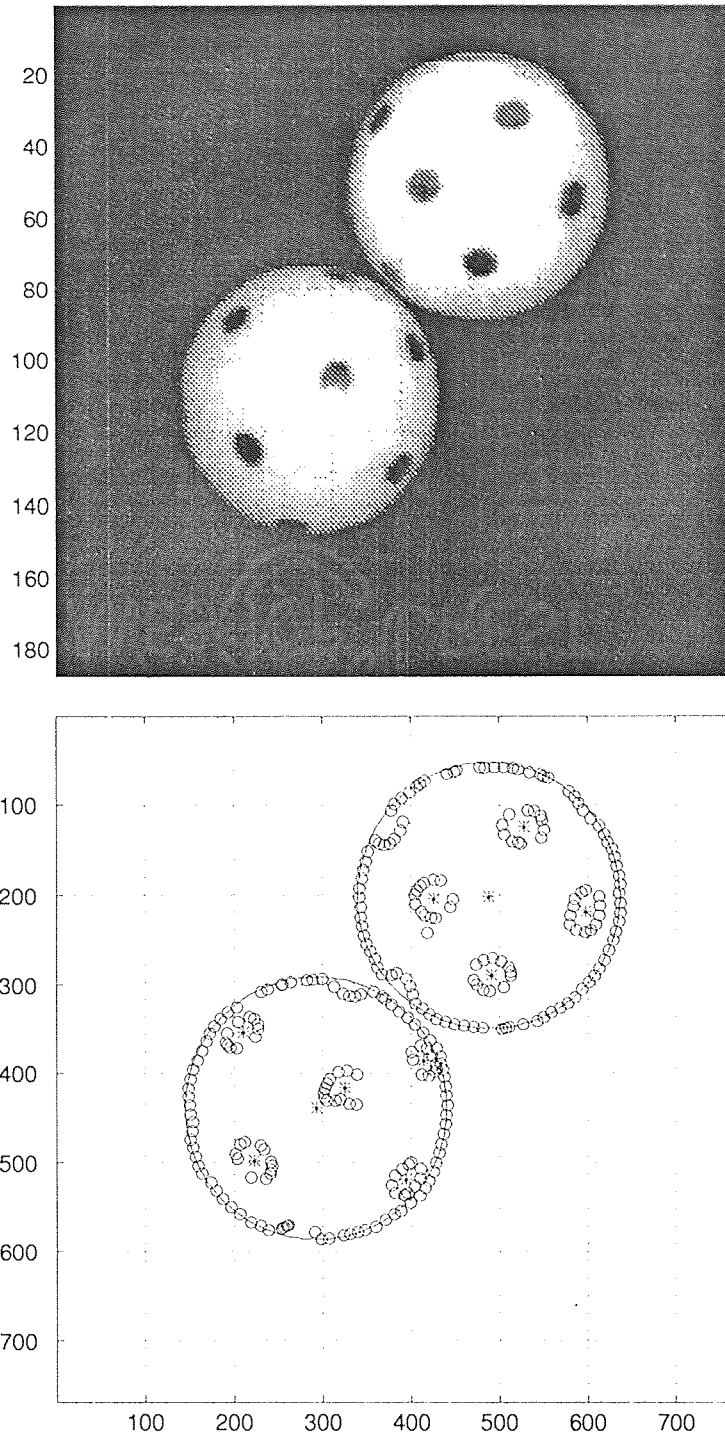
Figure 5.1 Gray level image (top) and corresponding *edge* image obtained after processing. The circles (o) are edge points and the stars (⋆) are the centers of the detected clusters (sphere or marker boundary).
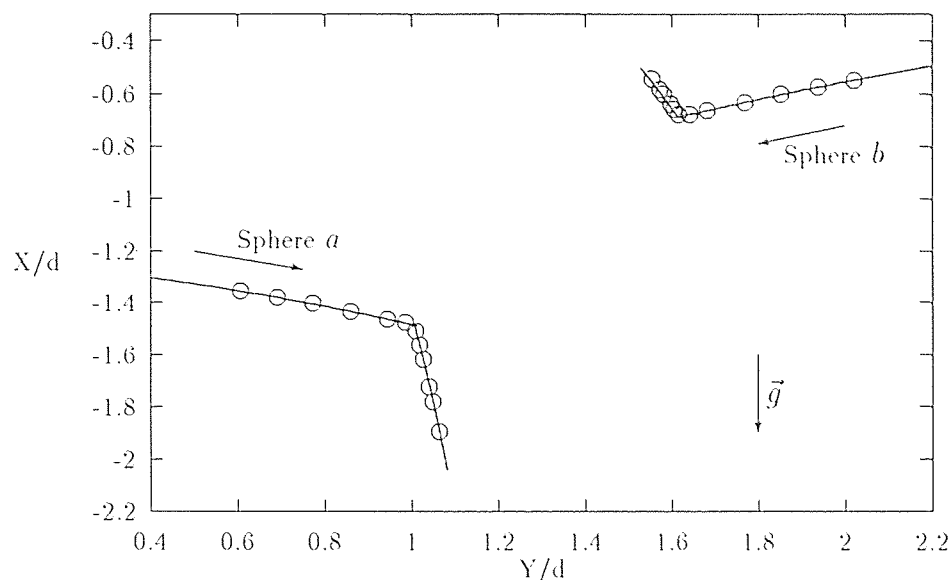
Figure 5.2 Motion of two colliding spheres a and b before and after collision. The position of the centers of the spheres are marked by the circles (o) while the solid lines represent the quadratic best fits of these positions in time.

the first time derivative of the parabolic fits. We find respectively for the x and y components of the velocities: $\sigma_{v_x} \simeq \sigma_{v_y} \simeq 4\,cm.s^{-1}$. For the radius of the spheres we find: $R = 148.7 \pm 1.77$ subpixel units. The instant at which the collision takes place is obtained by extrapolation from the fits using the value of R above. It is computed from the two pre-collision fits and from the two post-collision fits independently. In this particular experiment the two values of the time of collision were found to lie 0.1 ms apart. The effective accuracy of the location of the sphere centers is of the order of one or two subpixels, which is satisfactory as the occlusion of the contours of the markers often perturb the shape of the sphere boundaries. It is important to understand the consequences of this limited resolution on the ability of the whole experimental method to yield good kinematic measurements. As a rule of thumb, we expect that if the average time interval between frames is Δt, then the standard deviation obtained on a velocity component, say in the x-direction, will be related

to the standard deviation of the x coordinate of a sphere center according to:

$$\sigma_{v_x} \simeq \sigma_x / \Delta t$$

This can be checked in the above experiment where we find on average that $\sigma_{v_x} / (\sigma_x / \Delta t) \simeq 1.2$. Owing to the fact that σ_x depends only on the accuracy of the clustering algorithm and the number of frames used, it is a measure of absolute uncertainty which, as we will see further in this section, imposes pratical limitations on the experiment as far as the choice of the sphere sizes and velocities are concerned. To see this let us consider the collision of two 2.54 cm diameter spheres. Since we use a four-subpixel expansion (see section 4.4.1), the subpixel images have dimensions $L_h \times L_v$, where $L_h = 4 \times 240 = 960$ is the horizontal dimension and $L_v = 4 \times 192 = 768$ the vertical dimension. The scaling relation between the physical dimensions of the collision scene and those of the images is the number of subpixels per diameter which we call n_s. The time interval between two consecutive images is $q\delta t$ where $\delta t = 1\,ms$ and q is an integer equal or greater than one. Because we need to keep the number of images per collision within reasonable limits as far as processing time is concerned, q is sometimes larger than one. Finally let us assume that the spheres are travelling with a typical velocity v expressed in meters per second and that the uncertainty on the determination of each coordinate is of s subpixels. Let $\delta \vec{r}$ be the typical relative translation of the spheres between two consecutive frames, then we may conservatively estimate the relative error made on the measurement of the component of relative velocity $\vec{v}$ in a given direction ξ as:

$$\frac{\Delta v_\xi}{v_\xi} = \frac{s}{\delta r_\xi} = \frac{s}{\frac{v_\xi}{d} n_s q \delta t \sqrt{N}} \tag{5.1}$$

where the factor $\sqrt{N}$ (N is the average number of frames before or after collision) is included in a statistical sense to account for the decrease of the standard deviation of our measurements with the increasing number of frames used for a fit. The above expression shows how optimization of the error depends on the velocity of the spheres,

on their relative velocity and orientation and on their size. q and N are dependent parameters and are also imposed by the velocities, the relative velocity and the size or the ratio n_s/d. Equation 5.1 tells us that when v_ξ goes to zero the relative error goes to infinity because we cannot increase N or q infinitely. On the other hand, when v_ξ becomes very large N decreases because the spheres spend less time in the field of view and the relative error becomes infinite in this case too. Since we are interested in the values of normal and tangential relative velocities, the previous discussion implies that the latter are determined with the same accuracy and the relative error therefore diverges for the normal component in grazing impacts, while it diverges for the tangential component in head-on collision. Although the estimate given by Equation 5.1 is mostly qualitative, we can try and see how it compares with results obtained from a set of 16 test experiments performed with varying angles of incidence. We compare the prediction of Equation 5.1 with the computed relative variation of the total linear momentum. In that case, we used: $s = 2, q = 2, n_s \simeq 150$ and $N=5$, for which values Equation 5.1 predicts $\delta v_\xi / v_\xi \simeq 3/v_\xi$. The results are shown on Figure 5.3 where the solid line is the plot of $2/v_\xi$. As expected Equation 5.1 seems to be a reliable and conservative estimate of the relative error which therefore shows that the expected accuracy is controlled essentially by the resolution of the camera and that of the image processing techniques.

5.1.2 Rotational Motion and Out-of-plane Translation

The method used for determining the rotational velocities is borrowed from [65] and unchanged. It is also a least-squares technique which computes one rotation vector between two successive frames. The rotation vector at collision is taken to be the algebraic mean of all the inter-frame rotation vectors. Preliminary precision tests were reported in [65] concerning this technique. For the same reason as explained in Section 5.1.1, they apply only to very limited experimental conditions. The ability in
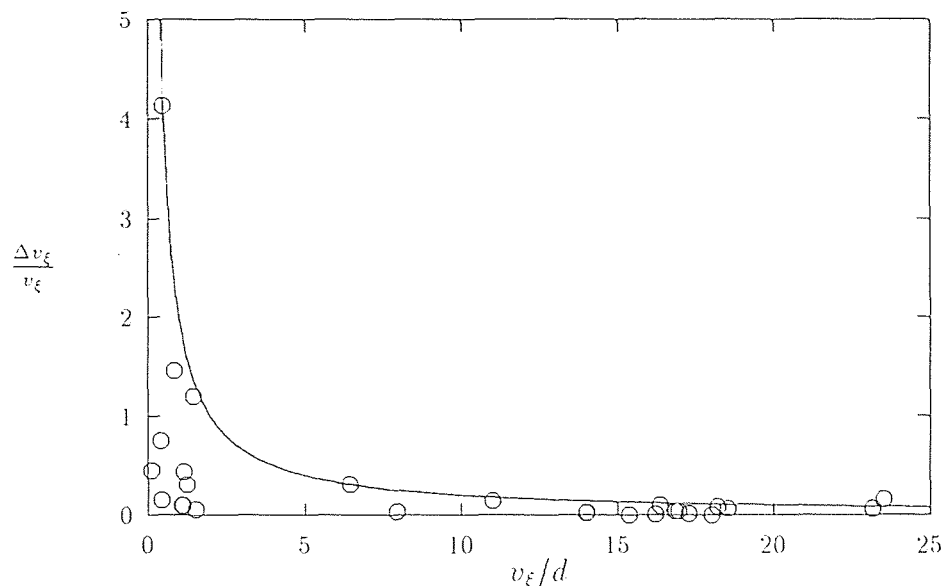
Figure 5.3 Relative error made on any velocity component versus its amplitude (expressed in units of sphere diameter per second). The solid line is $2/v_\xi$.

determining the three components of the rotation vector first depends on the accuracy with which the center of the sphere is tracked. On the other hand, and similarly to what happens in the case of the translation vector, the relative accuracy decreases with the amplitude of a given component of rotation. However we may hope that the magnitudes (or the angles of rotation) will be computed with more precision than the individual components of rotation. For the same test experiment shown in Section 5.1.1 we plot in Figures 5.4 and 5.5, respectively for sphere a and sphere b (see Figure 5.2) the three components of the rotation vector and its magnitude versus time. These plots evidence that the z-component (i.e. the rotation about the z-axis) is much larger and that, like the rotation velocity, it fluctuates much less than the x and y components. Also one can notice that the z-components of rotation of the two spheres are very close in magnitude and have opposite signs and therefore probably provide a negligible contribution to the relative velocity. We check these results on the same set of test experiments as used in Section 5.1.1 by studying
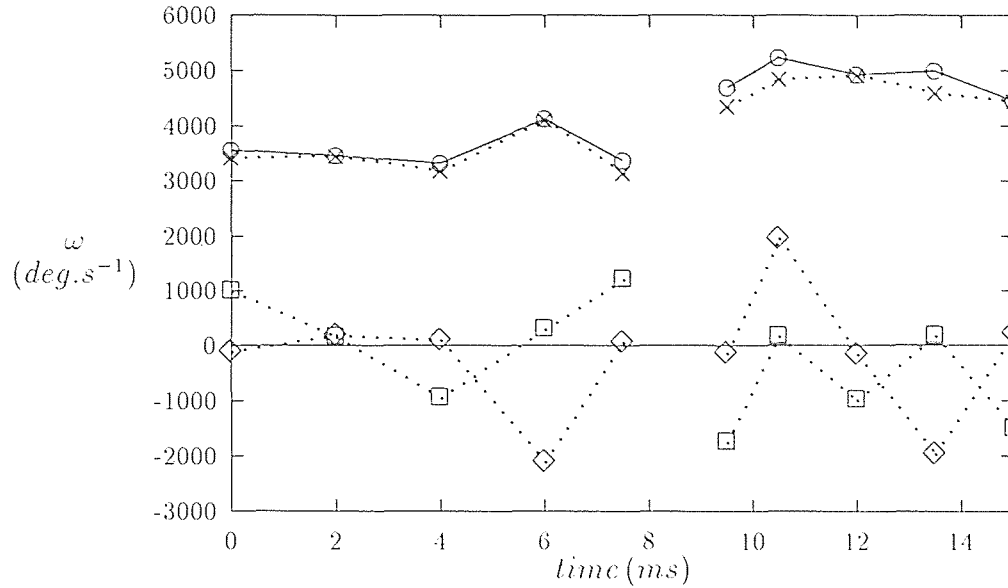
Figure 5.4 Measurements of average rotation between successive frames obtained from the test experiment for sphere a. The dotted lines are the components of the rotation vector: ω_x ($\diamond$), ω_y ($\square$), ω_z ($\times$). The solid line joining the circles (o) is the rotation speed. The split in the figure is due to the fact that we do not compute the rotation between the two frames immediately before and after the collision occurring between t=8 and t=9 ms.
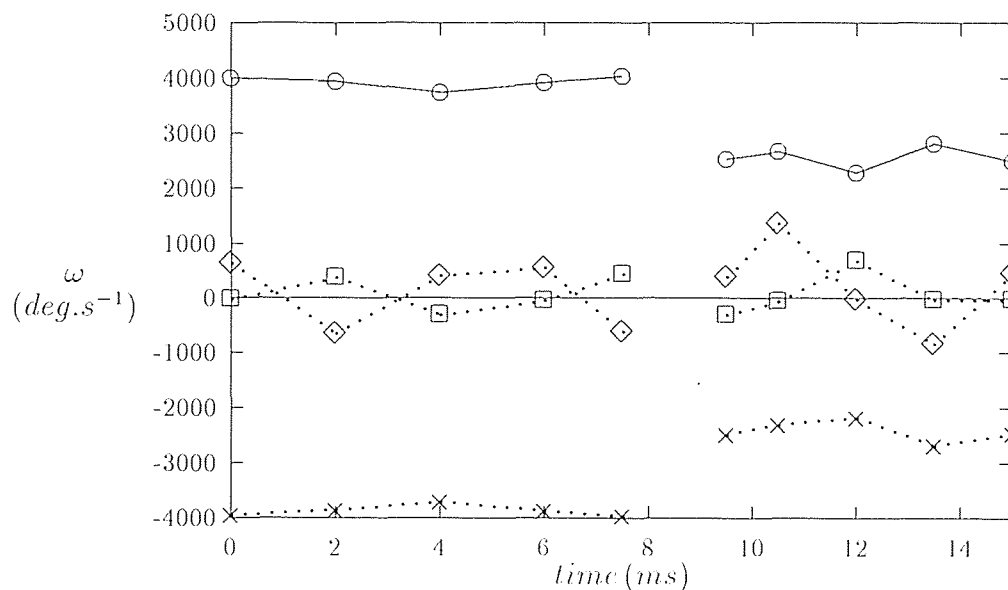

Figure 5.5 Measurements of rotation obtained from the test experiment for sphere b. Same symbols as in Figure 5.4.

the contribution of rotations to the relative tangential velocity. Results are shown in Figure 5.6 where we plot $\frac{a}{2}((\omega_{1x} + \omega_{2x})^2 + (\omega_{1y} + \omega_{2y})^2)^{\frac{1}{2}}/v_s$ and $\frac{a}{2}|\omega_{1z} + \omega_{2z}|/v_s$ versus the angle of incidence. As expected, rotations become very important at low incidence angles and otherwise $(-v_s/v_n)$ account for a few percent of v_s only. In fact, with the velocity range used in these experiments, their contribution (which is overestimated in Figure 5.6 because we take into account the torsional component, i.e. the component of $(\vec{\omega}_1 + \vec{\omega}_2)$ which is parallel to $\vec{n}$) is comparable to the uncertainty obtained in the previous section. In any case the the z-components of rotation contribute very little to the relative velocity.

The last unknown component of post-collisional translational velocity is that perpendicular to the focal plane, in the z-direction. It is obtained from the conservation of angular momentum once the change of linear momentum has been determined from the translational data. It is therefore computed with much less accuracy than the x and y components. The computation is done according to Equations B.1 and B.2. As mentioned in Chapter 4, the alignment of the tubes allows us to overlook the non-zero value of v_z before collision considering the expected accuracy of the two other components. However, since there is no control on the rotation vector, upon emergence from the end of the tubes, there is no reason why it should remain so after collision. Figure 5.7 shows the ratio $\mathcal{R}$ of the relative translational velocity perpendicular to the focal plane, V_z, to the normal or tangential component of relative velocities. This contribution is not significant because it lies within the domain of uncertainty evidenced in section 5.1.1.

5.1.3 Conclusion

For our purpose when using 2.54 cm diameter balls, typical velocities of $1\ m.s^{-1}$ can be measured within 5%. For this fixed value of translational velocity, when the angle of incidence is reduced so that the ratio $-v_s/v_n$ falls below 0.25, the relative tangential
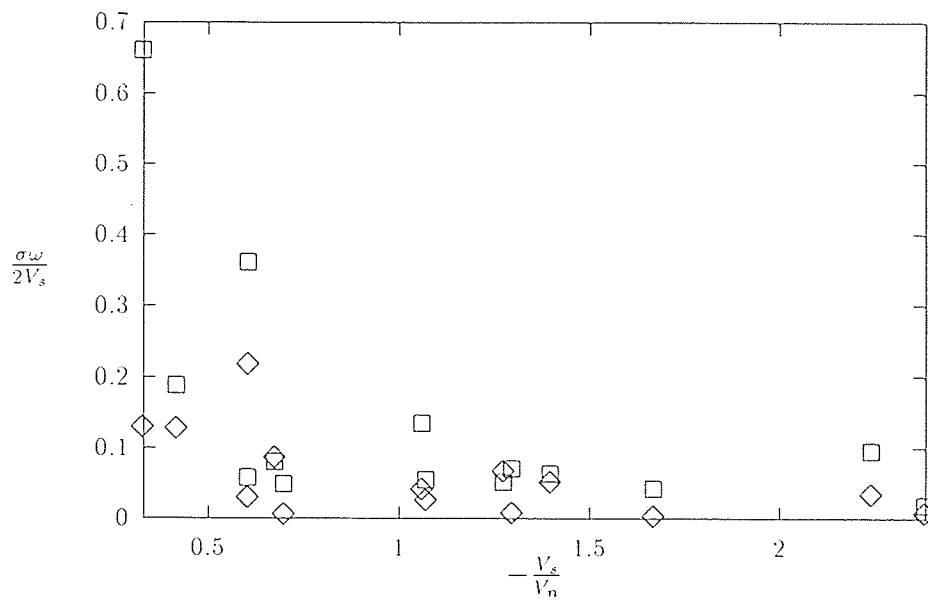
Figure 5.6 Estimation of the contribution of rotations to the relative velocity. z-component (perpendicular to the image) ($\Diamond$); x and y components ($\Box$).
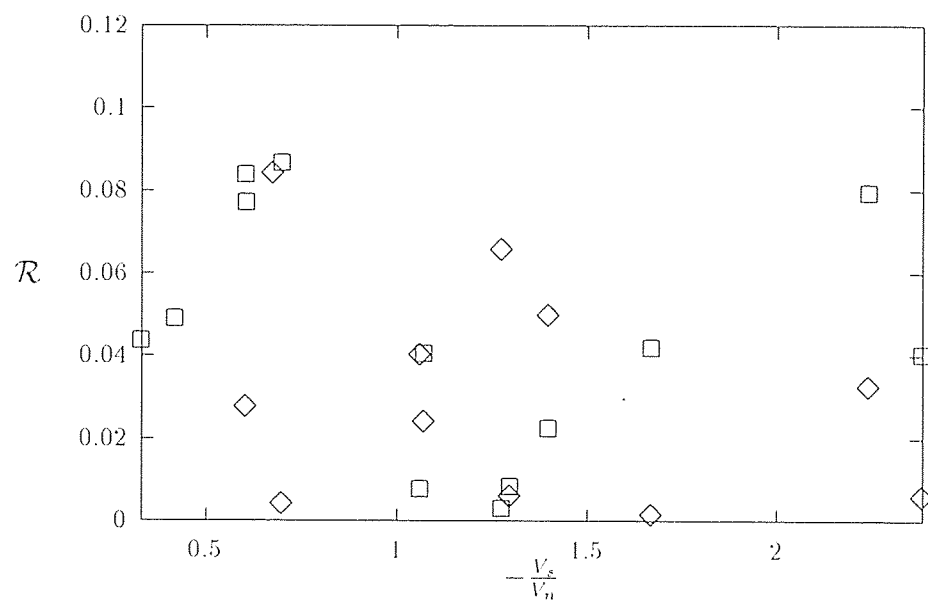

Figure 5.7 Normalized relative translational velocity: $\frac{V_z}{V_s}$ ($\Box$); $\frac{V_z}{V_n}$ ($\Diamond$).

velocity v_s is smaller than approximately 0.25 $m.s^{-1}$ and is therefore computed with 20% relative error. The same diagnostic applies for the normal component of relative velocity v_n for values of v_s/v_n larger than 4. Higher velocities or less frequent image sampling will provide better accuracy.

5.2 Collision Properties

In order to test the validity of Equations 3.5 and 3.4, we perform a series of collisions with two identical one inch diameter nylon spheres. For these experiments, the pressure level used to expel the spheres out of the tubes was kept constant, but the angle of incidence was varied by moving the right tube vertically. For this particular set of results, considering the study carried out in Section 5.1, we increase the release velocity of the spheres to about 1.2 $m.s^{-1}$, producing normal velocities at impact in the range 0.1 - 2.5 m/s. This corresponds to velocities 4 times larger than in Section 5.1 and therefore to a corresponding decrease of the relative error (see section 5.1.1). We used an average of 6 to 8 images before and after collision. Values of $-v_s'/v_n$ versus $-v_s/v_n$, where primed quantities are taken after a collision as in Chapter 3, are reported on Figure 5.8. The points reported qualitatively agree with the predictions of the collision operator presented in Chapter 3: Beginning from zero on the $-v_s/v_n$ axis, the tangent of the recoil angle $-v_s'/v_n$ first takes decreasing negative values indicating that the surface velocity $\vec{v}_s$ changes direction during the contact (see Equation 3.3). When $-v_s/v_n$ reaches a value of about 0.8 this trend changes and the recoil angle increases linearly as a first approximation.

For the same data we report directly the coefficient of tangential restitution as a function of $-v_n/v_s$ on Figure 5.9 where it can be seen that β seems to reach a plateau as actually assumed in Walton's operator in the rolling regime but tends to decrease as the surface velocity at impact decreases, i.e. when the collision is closer to a normal impact. We fit a straight line on the points of Figure 5.9 for values of $-v_n/v_s$ smaller
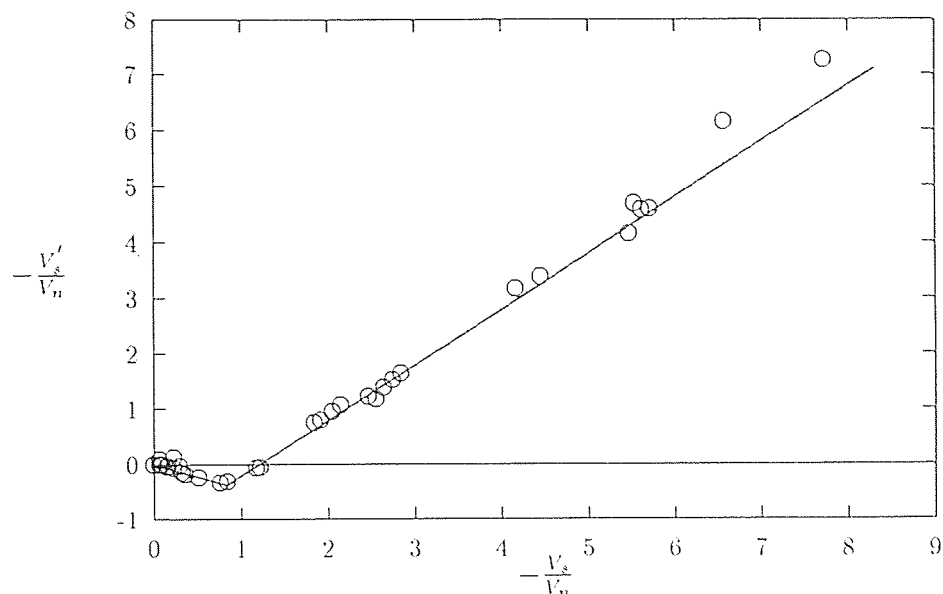
Figure 5.8 Tangent of the collision angle before versus after collision(o).

than 1.5, which we consider to be the *sliding* region. According to Equation A.10, the

slope, in Figure 5.9, of this *sliding* region is equal to $\frac{7}{2}\mu(1+e)$. We therefore measure:

$\frac{7}{2}\mu(1+e) = 1.21 \pm 0.01$. The value of β_0 is estimated at $\beta_0 = 0.44 \pm 0.04$ from the

same graph.   The coefficient of restitution e is obtained by averaging results

(i.e. measurements of $-v'_n/v_n$) of individual experiments and is found to be equal to

0.97 ± 0.015. However as shown on Figure 5.10, e decreases with increasing angle of

incidence. Therefore the above value of e was obtained for values of $-v_s/v_n$ lower

than 2. This behavior seems to go against previous observations by Sondergaard

et al. [56] and experimental results reported by Brach [47] for spheres impacting

plates.   Finally we can extract the coefficient of friction: $\mu = 0.176 \pm 0.015$. The

solid lines on Figure 5.9 and 5.8 are the solutions corresponding to Equations 3.5

and 3.4 of Walton's operator. Alternatively, β_0 and μ can in principle be extracted

from a plot of the impulse ratio f versus $-v_s/v_n$ by using Equations refimpulseratio.

Accordingly we compute the impulse ratio directly, using Equations A.1 and A.11,

and reported on Figure 5.11 along with the best fits taken from Figure 5.9.
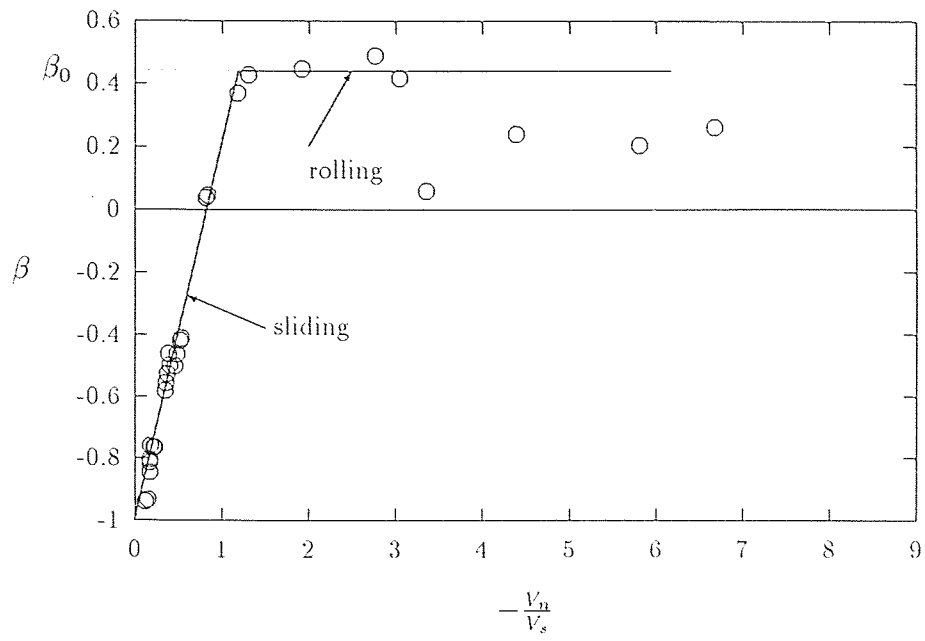
Figure 5.9 Coefficient of tangential restitution β versus the cotangent of the angle of incidence.
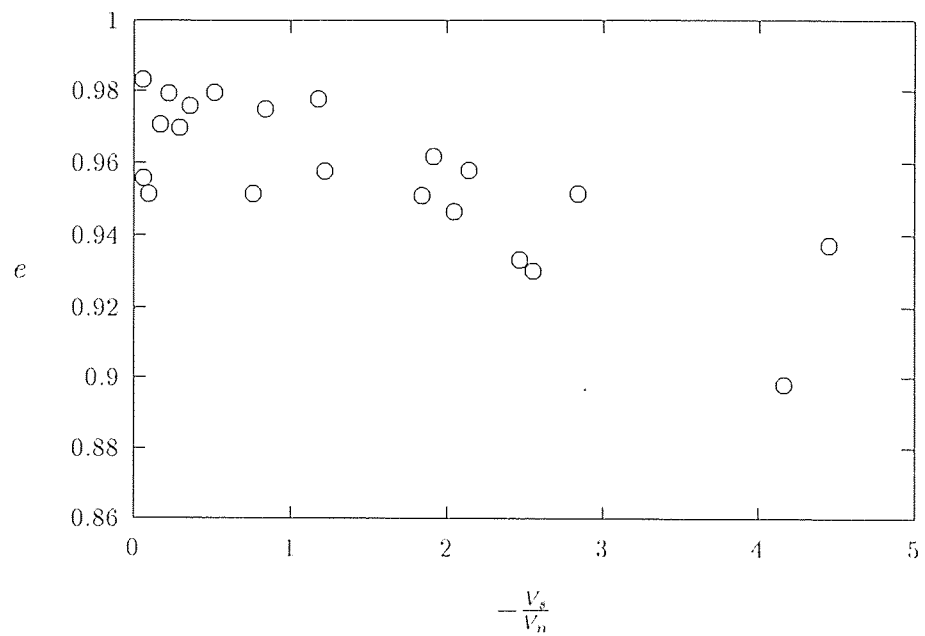
Figure 5.10 The coefficient of restitution versus the tangent of the angle of incidence.
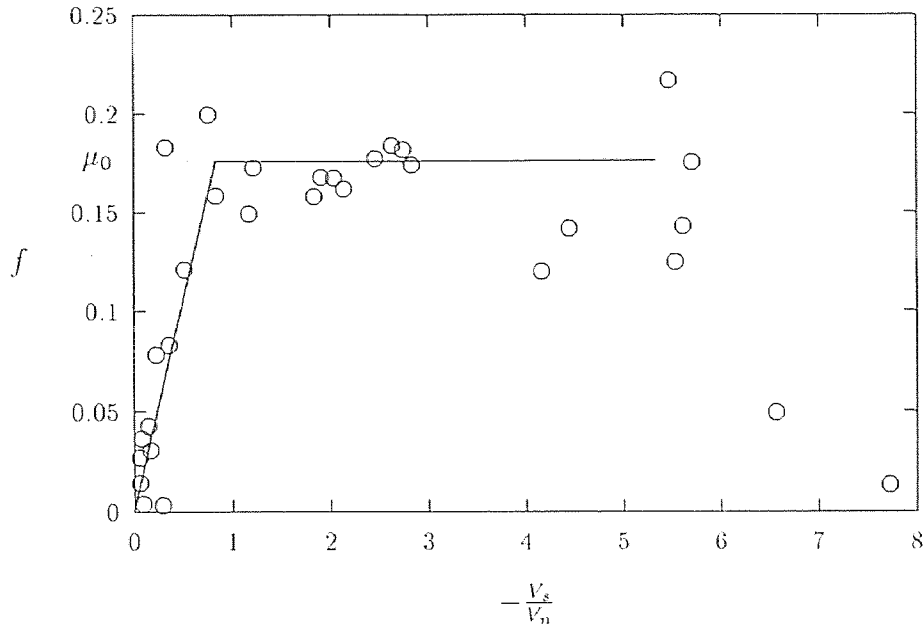
Figure 5.11 The impulse ratio f versus the tangent of the angle of incidence.

The *sliding* branch of Figure 5.8 seems to deviate from the the prediction of the operator for large incidence angles. This comes from the fact that μ was determined from a linear fit in the sliding regime of Figure 5.9 where β which was constrained to go through the point $(-\frac{v_s}{v_n} = \infty; \beta = -1)$. By doing so, we measured collision properties for intermediate angles of incidence (typically for $-v_s/v_n$ between 0.25 and 5 which corresponds to angles between 14° and 80°). The three collision properties are therefore well defined over a fairly wide range of incidence angles (i.e. 15° to 80°). In extreme impact geometries such as nearly head-on or grazing incidences, errors arising from experimental measurements do not allow us to test the model equations and to measure precisely the impulse ratio and the coefficient of restitution, respectively for large and very small incidence angles. Finally, in their analysis, Maw et al. [39] predict the occurrence of micro-slip for very small angles of incidence. Precisely, this would yield negative values of β for $-v_s/v_n \leq \mu(2-\nu)/2(1-\nu)$ which is about 0.21 if we assume a Poisson ratio ν of 0.3. Our experiment does not allow us to verify this prediction accurately. However, as mentioned above, values of β

reported on Figure 5.9 actually seem to decrease again for small angles of incidence (large values of v_n/v_s) and do not stand in contradiction with the possible occurence of a *micro-slip* region. They also find that when $-v_s/v_n \geq \mu(12 - 13\nu)/2(1 - \nu)$ (which is a number close to one for $\nu = 0.3$ and corresponds to an angle a little larger than 45°) gross-slip will persist throughout the impact. This is compatible with the value of γ_0 (see Appendix A) that we find to be approximately 40°.
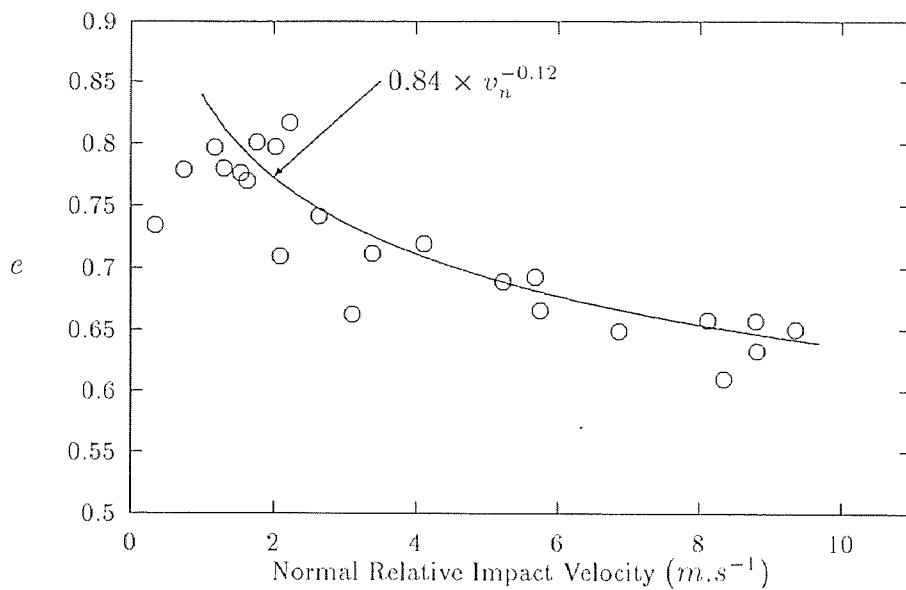
5.3 Coefficient of Restitution

As mentioned in Chapter 4, the experimental apparatus allows us to vary the exit velocity of the spheres thanks to the variable air pressure at the end of each tube. This was used to investigate the velocity dependence of the coefficient of restitution. In order to obtain maximum accuracy on the trajectory of the spheres, the latter were not marked with black dots in most of the experiments whose results are reported here, so as to avoid deformation of their contours (see Chapter 4). Figure 5.12 shows measured values of e for 1" and 0.5" diameter nylon spheres versus the magnitude of the normal component of relative impact velocity. Although for both sizes e is clearly a decreasing function of the impact velocity, starting from 1 at low velocity magnitudes, the scatter obtained shows that the accuracy of our measurement is not sufficient to predict any size dependence for the two sizes used. Such a comparison for the material used here would require measurements of e within less than a percent, as our measurements may be confounded due to fluctuations of the angle of incidence as shown in Figure 5.10. Furthermore if any mass dependence does exist it can only be very weak which is in agreement with the only previous observations reported in [43].

In both cases, the decrease appears to be much slower than the two theoretical power laws presented in [45] and [46]. The same experiments were performed for 1" teflon spheres and results are reported on Figure 5.13. Here the decrease of
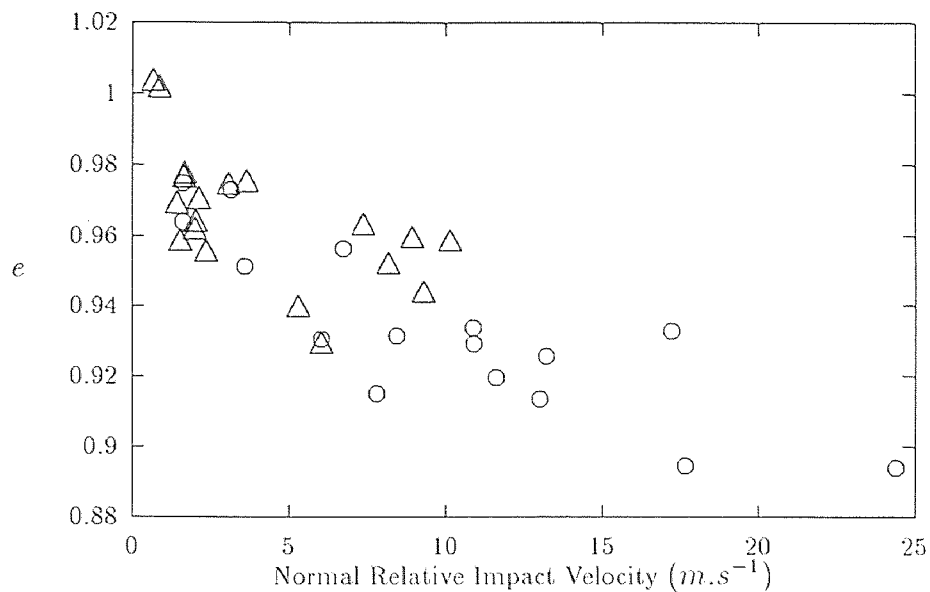
Figure 5.12 Coefficient of restitution (e) versus normal impact velocity for 2.54cm (△)and 1.27cm (o) diameter Nylon spheres.

Figure 5.13 Coefficient of restitution (e) versus normal impact velocity for 2.54cm (o) diameter Teflon spheres.

e is sharper and appears also quite scattered. A power-law behavior as indicated by the solid line in Figure 5.13, seems to be a good description of the data with a exponent of order 0.12 which is half that predicted by Ning et al. [46] and Johnson [40]. The possibility of a coupling between the normal and tangential deformation for elastic spheres has been refuted (see for example [40]), but it is not excluded that the existence of a zone of plastic deformation near the contact patch might affect the elastic properties of the material. However there are no available theoretical results to compare with and we do not know to what extent this assumption could be relevant. Also since we do not have a precise control of the angle of incidence at collision, a systematic study could be done only by carrying out a large number of experiments.

CHAPTER 6

CONCLUSION

An experimental apparatus along with the necessary image processing techniques were designed to investigate collision properties of spheres. It allowed us to make direct measurements of these properties on the basis of a simple collision operator. In contrast to previous experiments [55], it does not impose any constraints on the pre-collisional velocities and spins except that the pre-collisional trajectories of the two spheres have to lie in the same plane. Although measurements made at very low or very high incidence angles are not fully reliable, our results seem to show that there exists in both conditions a more detailed behavior as that assumed in Walton's collision operator. However the decrease of the coefficient of friction for increasing angle of incidence can be due to the existence of dust on the surfaces of the spheres or to cratering and is therfore mostly unpredictable. This can therefore lead to unpredictable fluctuations of either μ or β_0. The accuracy has been shown to be well controlled by the exact conditions in which a given experiment was performed, i.e. angle of incidence, velocities and size of the objects. Within our accuracy we can consider that this setup, although quite rudimentary, produces repeatable experiments.

Although we failed to provide conclusions on the mass dependence of the coefficient of restitution, we showed by experimenting on spheres with a mass ratio of 1/8 that if it existed it was to a very limited extent. The influence of the impact velocity, which did not reproduce any of the theoretical predictions that we know of, was different for the two kinds of materials we used in that the decrease observed for Teflon was much sharper as that of Nylon. For comparison with existing theoretical power laws, we found an exponent of 0.12 for Teflon which is half the predicted value. However a precise measurement of such an exponent would require an extension of the velocity range by another order of magnitude. Finally, the setup could be used

47

to further investigate the dependence on the impact velocity of the coefficient of restitution in the optimal experimental conditions studied in Chapter 5 and is likely to produce more conclusive results for softer materials.

APPENDIX A

Derivation of Walton's Collision Operator

Here we will present a derivation of Equations 3.5 and 3.4. The notations are therefore the same as in Chapter 3.

The impulse exerted by sphere one on sphere two, $\Delta \vec{P}$, relates pre- and post-collisional velocities and rotations according to:

$$\Delta \vec{P} = m_1(\vec{v}_1' - \vec{v}_1) = -m_2(\vec{v}_2' - \vec{v}_2) \tag{A.1}$$

and

$$-\vec{n} \times \Delta \vec{P} = \frac{2 I_1}{\sigma_1}(\vec{\omega}_1' - \vec{\omega}_1) = \frac{2 I_2}{\sigma_2}(\vec{\omega}_2' - \vec{\omega}_2) \tag{A.2}$$

Using Equation 3.1, we may express the change in sliding velocity occurring during collision as:

$$\vec{v}_c' - \vec{v}_c = (\vec{v}_1' - \vec{v}_1) - (\vec{v}_2' - \vec{v}_2) - [\frac{\sigma_1}{2}(\vec{\omega}_1' - \vec{\omega}_1) + \frac{\sigma_2}{2}(\vec{\omega}_2' - \vec{\omega}_2)]\vec{n} \tag{A.3}$$

Upon inserting Equations A.1 and A.2 in Equation A.3, this change is now obtained in terms of $\Delta \vec{P}$ as:

$$\vec{v}_c' - \vec{v}_c = \frac{7}{2}\frac{\Delta \vec{P}}{m_{12}} - \frac{5}{2}\frac{\Delta \vec{P}_n}{m_{12}} \tag{A.4}$$

where $\Delta \vec{P}_n = (\Delta \vec{P} \cdot \vec{n})\vec{n}$ is the momentum change in the normal direction. By using the definition of the cofficient of restitution given by Equation 3.2, this component of momentum change can be rewritten as:

$$\Delta \vec{P}_n = -m_{12}(1 + e)\vec{v}_n \tag{A.5}$$

If it is assumed that sliding occurs throughout the impact then the two components of impulse are related by:

$$\Delta \vec{P}_t = -\mu_0 |\Delta \vec{P}_n|\vec{t} \tag{A.6}$$

where $\vec{t} = \vec{v}_s/|v_s|$ is a unit vector with the direction and orientation that the relative surface velocity had before contact. Therefore:

$$\Delta \vec{P}_t = \mu_0 m_{12}(1 + e)\cot\gamma\,\vec{v}_s \tag{A.7}$$

Since $\pi/2 \le \gamma \le \pi$, as may be seen on Figure 3.2, $\cot\gamma \le 0$. After substitution of Equations A.5 and A.7 into Equation A.4, we find:

$$\vec{v}_c' - \vec{v}_c = -(1 + e)\vec{v}_n + \mu_0(1 + \frac{1}{K})(1 + e)\cot\gamma\,\vec{v}_s \tag{A.8}$$

For real contacts during which sliding ends before separation of the two bodies Coulomb's law is not valid anymore, e.g. $|\Delta \vec{P}_t| \le \mu_0|\Delta \vec{P}_n|$. In this case (*rolling*), $\beta = \beta_0$, i.e:

$$\vec{v}_s' = -\beta_0\,\vec{v}_s \tag{A.9}$$

Next Equations A.9 and A.8 are rewritten by projecting each of them along $\vec{t}$ to yield Equations 3.5 and 3.4. Comparison of A.9 and A.8 gives the dependance of β upon the ratio v_n/v_s:

$$\beta = -1 - \mu_0(1 + \frac{1}{K})(1 + e)\frac{v_n}{v_s} \qquad for\ \gamma \le \gamma_0$$
$$\beta = \beta_0 \qquad for\ \gamma \ge \gamma_0 \tag{A.10}$$

where γ_0 is given by $\tan\gamma_0 = \mu_0(1 + \frac{1}{K})\frac{1+e}{1+\beta_0}$. Similarly, Equations A.10 may be inverted to find the impulse ratio

$$f \overset{def}{=} \frac{|\Delta \vec{P}_t|}{|\Delta \vec{P}_n|} \tag{A.11}$$

(where $\Delta \vec{P}_t = \Delta \vec{P} \cdot \vec{t}$ and $\Delta \vec{P}_n = \Delta \vec{P} \cdot \vec{n}$) for any angle of incidence:

$$f = \mu_0 \qquad for\ \gamma \le \gamma_0$$
$$f = -(1 + \frac{1}{K})^{-1}\frac{1 + \beta_0}{1 + e}\frac{v_s}{v_n} \qquad for\ \gamma \ge \gamma_0 \tag{A.12}$$

Finally we can see, for example in Equation A.10, that if Coulomb's law was applied for any angle of incidence γ, then β would diverge to infinity as v_s would decrease.

This is why a coefficient of maximum tangential restitution β_0 is naturally defined, imposing an upper bound on the restitution of energy in the tangential direction.

APPENDIX B

Computation of the Out-of-plane Translational Velocities

In order to obtain the z-component of the velocities of the spheres, after collision it is assumed first that their trajectories prior to collision are perfectly aligned in a vertical plane so that unit vector $\vec{n}$ has components $(n_x, n_y, 0)$ and the velocity components of both spheres in the z-direction prior to collision, v_{1z} and v_{2z}, are zero as well. Here we also assume that the spheres are identical, each having mass m and diameter σ. From equation A.1 we therefore have:

$$v'_{1z} = -v'_{2z} = \Delta P_z / m \tag{B.1}$$

Projecting equation A.2 on the x and y axis, we obtain respectively:

$$-n_y \Delta P_z = \frac{\sigma m}{5} (\Delta \omega_{1x} + \Delta \omega_{2x})$$
$$n_x \Delta P_z = \frac{\sigma m}{5} (\Delta \omega_{1y} + \Delta \omega_{2y})$$

where

$$\Delta \omega_{i_\xi} = \omega'_{i_\xi} - \omega_{i_\xi}$$

for $i = 1, 2$ and $\xi = x, y$.

As long as n_x and n_y are non zero, ΔP_z can therefore be computed in four different ways. We choose to compute the following average of these terms:

$$\Delta P_z = \frac{\sigma m}{10(\alpha_x + \alpha_y)} \left(\alpha_x \frac{\Delta \omega_{1x}}{-n_y} + \alpha_x \frac{\Delta \omega_{2x}}{-n_y} + \alpha_y \frac{\Delta \omega_{1y}}{n_x} + \alpha_y \frac{\Delta \omega_{2y}}{n_x} \right) \tag{B.2}$$

where

$$\alpha_x = 0 \ \ if \ \ |n_y| \leq 0.1 \, |n_x|$$
$$= 1 \ \ otherwise$$
$$\alpha_y = 0 \ \ if \ \ |n_x| \leq 0.1 \, |n_y|$$
$$= 1 \ \ otherwise$$

REFERENCES

1. O. Reynolds. Phil. Mag. **20**, 469 (1885).

2. H. M. Jaeger and S. R. Nagel, Science **255**, 1523 (1992); H.M. Jaeger, J.B. Knight, C. H. Liu and S.R. Naegel, MRS Bulletin **5**, 25 (1994).

3. A.D. Rosato, K.J. Strandburg, F. Prinz and R.H. Swendsen , Phys. Rev. Lett. **58**, 1038 (1987).

4. A.D. Rosato, K.J. Strandburg, F. Prinz and R.H. Swendsen , Powder Techn.**49**, 59 (1986).

5. F. Cantelaube, PhD Dissertation, University of Rennes, France (1995).

6. R. Jullien, P. Meakin and A. Pavlovitch, Phys. Rev. Lett. **69**, 640 (1992).

7. J. Duran, J. Rajchenbach and E. Clément, Phys. Rev. Lett. **70**, 2431 (1993).

8. J. A. C. Gallas, H. J. Herrmann and S. Sokolowski, Physica A **189**, 437 (1992).

9. H. K. Pak and R. P. Behringer, Phys. Rev. Lett. **71**, 1832 (1993).

10. F. Melo, P. Umbanhower, and H. L. Swinney, Phys. Rev. Lett. **72**, 172 (1994).

11. E. Clément, J. Duran and J. Rajchenbach, Phys. Rev. Lett. **69**, 1189 (1992).

12. C. Laroche, S. Douady, S. Fauve, J. de Physique **50**, 699 (1989).

13. R.A. Bagnold, Proc. R. Soc. Lond. **A225**, 49 (1954).

14. S.B. Savage, in *Theoretical and Applied Mechanics*, pp. 241-266, P. Germain, M. Piau and D. Caillerie (Eds.), Elsevier Science Pub., B.V. North Holland, (1989).

15. M.P. Allen and D.J. Tildesley, *Computer Simulation of Liquids*, Oxford University Press, Oxford (1987).

16. S.B. Savage, J. Fluid Mech. **92**, 53 (1979).

17. S.B. Savage and R. Dai, Mechanics of Materials **16**, 225 (1993).

18. O.R. Walton and R.L. Braun, J. of Rheol. **30**(5), 949 (1986).

19. O.R. Walton and R.L. Braun, Acta Mechanica **63**, 73 (1988).

20. C.S. Campbell and C.E. Brennen, J. Fluid Mech. **151** , 167 (1985).

21. C. S. Campbell, Annu. Rev. Fluid Mech. **22**, 57 (1990).

22. M.P. Allen and D.J. Tildesley, *Computer Simulation of Liquids*, Oxford University Press, Oxford (1987); J. A. C. Gallas, H. J. Herrmann and S. Sokolowski, Phys. Rev. Lett. **69**, 1375 (1992); P. A. Cundall and O. D. L. Strack, Géotechnique **29**, 47 (1979); Y.-h. Taguchi, Phys. Rev. Lett. **69**, 1371 (1992); J. Lee, J. Phys **27**, L257 (1994); J. Lee and H. J. Herrmann, J. Phys. A **26**, 373 (1993).

23. B.D. Lubachevsky, J. Comp. Phys, **94**, 255 (1991); S. McNamara and W.R. Young, Phys. Fluids A **4**, 496 (1992); S. McNamara and W.R. Young, Phys. Fluids A **5**, 34 (1992).

24. S. Luding, Phys. Rev. E **52**, 4442 (1995).

25. B.D. Lubachevsky, J. Comp. Phys, **94**, 255 (1991).

26. S. Luding, H. J. Herrmann, A. Blumen, Phys. Rev. E **50**, 3100 (1994).

27. P. K. Haff, J. Fluid Mech. **134**, 401 (1983).

28. J. T. Jenkins and S. B. Savage, J. Fluid Mech. **130**, 187 (1983).

29. C.K.K. Lun, S.B. Savage, D.J. Jeffrey and N. Chepurnity, J. Fluid Mech. **140**, 223 (1984).

30. S. Luding, E. Clément, A. Blumen, J. Rajchenbach and J. Duran, *Mat. Res. Soc. Symp. Proc* **367**, (1995).

31. O.R. Walton, Acta Mechanica **63**, 947 (1988).

32. S. Luding, E. Clément, A. Blumen, J. Rajchenbach, and J. Duran, Phys. Rev. E **50**, R1762 (1994).

33. L.D. Landau and E.M. Lifshitz, *Fluid Mechanics*, Pergamon Press, London (1959).

34. S. C. Hunter, Journal of Mechanics and Physics of Solids **5**, 162 (1957).

35. J. M. Lifshitz and H. Kolsky, Journal of Mechanical and Physical Fluids **12**, 35 (1964).

36. For a discussion of the validity of this assumption see Ref. [40].

37. R.D. Mindlin, J. Appl. Mech. (Trans ASME) **16**, 259 (1949).

38. R.D Mindlin and H. Deresiewicz , J. Appl. Mech. (Trans ASME) **21**, 237 (1953).

39. N. Maw, J.R. Barber and J.N. Fawcett, Wear **38** (1), 101 (1976).

40. K.L Johnson, *Contact Mechanics*, Cambridge Univ. Press, New York (1985).

41. N. Maw, J.R. Barber and J.N. Fawcett, J. Lub. Tech. (Trans ASME) **20**, 327 (1981).

42. W. J. Stronge, Proc. R. Soc. Lond. **A431**, 169 (1909).

43. W. Goldsmith, *Impact*, E. Arnold Pub., London (1960).

44. C.V. Raman, Phys. Rev. **12**, 442 (1918).

45. G. Kuwabara and K. Kono, Jpn. J. Appl. Phys. **26**, 1230 (1987).

46. Z. Ning and C. Thornton, in *Powders & Grains 93*, C. Thornton (ed.), Balkema, Rotterdam (1993).

47. R.M Brach, *Mechanical Impact Dynamics*, John Wiley & Sons Pub., New York (1991).

48. J.T. Jenkins and M.W. Richman, Phys. Fluids **28**, 3485 (1985).

49. C.K.K. Lun and S.B. Savage, J. Appl. Mech. **54**, 47, (1987).

50. J.T. Jenkins, ASME J. Appli. Mech. **59**, 120 (1992).

51. C.K.K. Lun and S.B. Savage, Acta Mech. **63**, 15 (1986).

52. O.R. Walton, in *Particulate Two Phase Flow*, ed. M.C. Roco (Butterworth-Heinemann, Boston 1992), pp. 884-907.

53. P. A. Cundall and O. D. L. Strack, Géotechnique **29**, 47 (1979).

54. J. Schafer, S. Dippel and D.E Wolf, J. Phys. I **6**, 5 (1996).

55. S.F. Foerster, M.Y. Louge, H. Chang and K. Allia, Phys. Fl. **6** 3 (1994).

56. R. Sondergard and K. Chaney, J. Appl. Mech. **57**(9), 694 (1990).

57. R.N. Dave, J. Yu and A. D. Rosato, *ASME WAM Symposium on Mechatronics*, DSC-vol.**50**/PED-vol.**63**, 217 (1993).

58. T.G. Drake and R. Shreve, J. Rheol **30**(5), 981 (1986).

59. T.G. Drake, J. Fluid Mech. **225**, 121 (1991).

60. A.D. Rosato and Y. Lan, in *Powders & Grains 93*, C. Thornton (ed.), Balkema, Rotterdam (1993).

61. H. Ahn, PhD Dissertation, California Institute of Technology, (1989).

62. S. Warr, G.T.H. Jacques and J.M. Huntley, Powder Technology, **81**, 41, (1994).

63. S. Warr, J.M. Huntley and G.T.H. Jacques, Phys. Rev. E **52**, 5583 (1995).

64. P. Evesque, Contemp. Phys. **33**, 245 (1992).

65. J. Yu, M.S. Thesis, NJIT, Newark, NJ (1993).

66. J. Volcy, Technical Report, NJIT, Newark, NJ (1991).

67. K. Bhaswan, M.S. Thesis, NJIT, Newark, NJ (1991).

68. S. Sen, M.S. Thesis, NJIT, Newark, NJ (1991).

69. A. Huertas and G. Medioni, IEEE Trans. on Pattern Analysis and Machine Intelligence, PAMI-**8**, 651 (1986).

70. J. Illingworth and J. Kittler, *IEEE T-PAMI* **5**, 690 (1987).

71. R.N. Dave, Int. J. of General Systems, **16**(4), 353 (1990).

72. R.N. Dave, Pattern Recognition Letters **12**(11), 657 (1991).

73. R.N. Dave, *IEEE International Conference on Fuzzy Systems*, San Diego, CA, March 8-12, p127 (1992).

74. R.N. Dave and K. Bhaswan, *IEEE T. on Neural Networks* **3**(5), 643, 1992.

75. R.N. Dave, *IEEE International Conference on Fuzzy Systems*, San Francisco, CA, March 28-April 1, 1281 (1993).